Numerical And Experimental Aerodynamic Investigation Of A Micro-UAV For Flying On Mars

Hervé Bézard, Thibault Désert, Thierry Jardin, Jean-Marc Moschetta

Numerical And Experimental Aerodynamic Investigation Of A Micro-UAV For Flying On Mars

Hervé Bézard
Research Engineer
ONERA
Toulouse, France

Thibault Désert
Dr.
ONERA
Toulouse, France

Thierry Jardin
Dr.
ISAE-SUPAERO
Toulouse, France

Jean-Marc Moschetta
Pr.
ISAE-SUPAERO
Toulouse, France

ABSTRACT

This paper presents a numerical and experimental investigation of the aerodynamic characteristics of a vertical take-off and landing micro air vehicle designed to fly in the Martian atmosphere. Numerical tools are validated through experimental data from the literature where Martian conditions are replicated. An innovative airfoil is designed for the specific flying conditions of the Martian MAV, i.e. compressible and ultra-low Reynolds number flows. This airfoil is evaluated in different Reynolds and Mach number conditions using unsteady compressible laminar Navier-Stokes simulations. Single rotors and coaxial configurations are designed for different thrust constraints by optimizing the chord and twist distributions using a free wake lifting line method. Rotors are firstly evaluated numerically using Navier-Stokes simulations. To validate the simulations, the optimized configurations are tested experimentally in an evacuation chamber, recreating Martian atmosphere in terms of density and gas. Thrust and torque on each rotor are measured by a two-component set-up. Tests are performed up to transonic flow conditions at blade tip. Results are extrapolated to a suggested design for a Martian MAV.

NOTATION

A	=	rotor disc area (m^2)	=	πR^2
AR	=	wing aspect ratio	=	span/chord
c	=	chord length (m)		
C_D	=	drag coefficient	=	$\frac{D}{\frac{1}{2}\rho S_{ref} V_{ref}^2}$
C_L	=	lift coefficient	=	$\frac{L}{\frac{1}{2}\rho S_{ref} V_{ref}^2}$
C_P	=	power coefficient	=	$\frac{P}{\rho A V_{tip}^3} = \frac{P}{\pi \rho \Omega^3 R^5}$
C_T	=	thrust coefficient	=	$\frac{T}{\rho A V_{tip}^2} = \frac{T}{\pi \rho \Omega^2 R^4}$
D	=	aerodynamic drag of a wing (N)		
FM	=	figure of merit	=	$\frac{C_T^{3/2}}{C_P \sqrt{2}}$
L	=	aerodynamic lift of a wing (N)		
M	=	Mach number		
M_{tip}	=	blade tip Mach number		
P	=	aerodynamic power of a rotor (W)		
R	=	rotor radius (m)		
Re	=	chord Reynolds number	=	$\frac{\rho V c}{\mu}$
S_{ref}	=	wing reference surface (m^2)		
T	=	aerodynamic thrust of a rotor (N)		
t/c	=	airfoil relative thickness (%)		
T/P	=	power loading (N/W)		
V_{ref}	=	reference velocity (m/s)		
V_{tip}	=	blade tip velocity (m/s)	=	ΩR
α	=	angle of attack		
γ	=	gas specific heat ratio		
μ	=	gas dynamic viscosity (Pa.s)		
ρ	=	gas density (kg/m^3)		
σ	=	rotor solidity	=	S_{rotor}/A
Ω	=	rotational speed (rad/s)		

INTRODUCTION

Until now, Martian surface exploration has been operated by rovers such as Curiosity or Opportunity. Rovers are limited in terms of range and accessibility. Only 60 km were explored on the 21,000 km of the circumferential path of the planet. Slow exploration rate is mainly due to the hilly landscape implying a limited traversable terrain for a rolling device and a lack of visibility on the ground. An aerial vehicle associated to a rover could significantly increase the global range and mobility by providing an aerial point of view of its upcoming pathway.

Several aerial vehicle technologies have been considered for this mission. A fixed-wing aircraft has the ability to map a large geographical area. However, the very low density of Mars' atmosphere compels this technology to high flying velocity which limits its maneuverability. Furthermore, it can hardly take-off from and land on the rocky ground of Mars, which limits its mission to one flight as in the ARES project of NASA (Braun, Ref. 1). A balloon is a compromise between aircraft and orbiters. This technology provides the possibility to fly several days at a few kilometer altitude covering thousands of kilometers of varied terrain (Kerzhanovich, Ref. 2). Yet, since balloon movement depends on atmospheric flows, it is sensitive to the severe winds blowing on Mars and the range of manoeuvers is limited. A vertical take-off and landing (VTOL) micro-aerial vehicle (MAV) seem to be the best suited aircraft for this mission compared to a fixed wing aircraft or a balloon. Such a drone could firstly be able to fly over the surrounding terrain of the rover for future paths exploration. It could also explore inaccessible places such as cliffs and canyons, and even land on the ground to retrieve

small samples of soil and get back for analysis by the rover. This advanced and original concept is investigated in different countries (USA, Japan, China, Europe) and space research institutes (NASA, JAXA, ESA). The most finalized concept of Martian helicopter will soon be launch by NASA/JPL with the Mars 2020 mission (Balaram, Ref. 3, 4). Its propulsion system is made of coaxial rotors of 1.2 m diameter and the drone weighs 1.8 kg. The energy used for flying and component warming is generated by a small solar panel on top of it, which limits its flight to less than 2 min per day.

In the present paper, a smaller vehicle design (30 cm diameter) is proposed. The small dimensions could facilitate swarming, maneuverability and interactions with the rover and, in a potential future, with humans. Such a MAV could easily take-off from and land on the rover to recharge and heat its batteries and exchange data or material collected in flight. So far, rover-drone interactions are prohibited by NASA for safety reasons. Hence, it could also land nearby and be picked up by means of a dedicated robotic arm, or be completely autonomous if equipped with an electric power supply like a solar cell.

Because of the characteristics of the Martian atmosphere, the drone's rotor blades rotate in compressible and ultra-low Reynolds number conditions. This is an innovative domain of aerodynamics and fluid mechanics, with very few available numerical and experimental data. Designing an aerodynamically efficient rotorcraft for flying these conditions is very challenging. Optimization of airfoil and rotor blade geometries is necessary to achieve sufficient thrust with minimum power for an instrumented Martian flight. In the literature, isolated rotor blade shape optimization based on the blade element momentum theory (BEMT) was achieved for $Re < 10{,}000$ by Kunz (Ref. 5), Liu (Ref. 6) and Bohorquez (Ref. 7). Airfoils were designed either by Xfoil, a simple panel method coupled with integral boundary layer method (Drela, Ref. 8), or by INS2D, an incompressible Navier-Stokes code (Kunz, Ref. 5). For the Martian helicopter concept, NASA used CAMRAD II, a free vortex method (FVM) to optimize the planform distribution of the two-bladed coaxial rotors (Balaram, Ref. 4). The coaxial rotor configuration is proven to be the most efficient propulsion system for a given size (Leishman, Ref. 9, and Song, Ref. 10).

Ultra-low Reynolds number conditions ($Re < 20{,}000$) can be found on nanorotors at ambient pressure or recreated in depressurized facilities. Bohorquez (Ref. 7) measured the performance of isolated nano rectangular blades for a tip Reynolds number $Re_{tip} < 20{,}000$ and the impact of spacing between upper and lower rotor in a coaxial configuration. Other authors investigated the influence of spacing of coaxial rotors in low Reynolds number flows through simulations (Lakshminarayan, Ref. 11) and experiments (Liu, Ref. 12). Concerning depressurized facilities, NASA was first to experimentally recreate the Martian atmospheric conditions in a depressurized chamber. They started by experimenting a four bladed rotor with linear twist distribution (Young, Ref. 13). The experiment was also simulated in 3D to investigate the flow behavior for $Re_{tip} > 60{,}000$ (Corfeld, Ref. 14). In the range $Re < 10{,}000$, the influence of airfoils, span, curvature, taper, Reynolds number, blade incidence, rotational speed and advance ratio were experimentally measured in different depressurized facilities (Shrestha, Ref. 15, Munday, Ref. 16, Tsuzuki, Ref. 17 and Ament, Ref. 18).

For a full understanding of the aerodynamic challenges faced by a Martian MAV, there are still many points to address. BEMT and FVM have not yet been fully evaluated in compressible ultra-low Reynolds flows contrarily to high fidelity solvers (Ref. 24). No optimization of the full propulsion system based on FVM has been carried out for now. No investigation provides 3D validated CFD simulations of the experimentally evaluated rotors in the range of Reynolds number of the Martian MAV corresponding to fully laminar flows. Experiments have not been carried out up to transonic conditions at blade tip. The present paper fills up the missing knowledge about the physical phenomenon faced by a Martian helicopter and proposes a novel design based on aerodynamic optimization. After a brief presentation of the Martian atmosphere characteristics and aerodynamic conditions faced by the blade flow, Navier-Stokes solver is evaluated on a referenced experiment from the literature. The optimization process of the blade airfoil is then presented and its performance is evaluated with the validated solver for a large range of Mach and Reynolds numbers. Single rotor geometries are optimized using BEMT and FVM, and several lower rotors are optimized for several coaxial configurations (depending on the aimed thrust) taking into account the interaction with the wake of the upper rotor. Rotor geometries are investigated numerically with the validated Navier-Stokes solver and experimentally. Experiments are carried out in ONERA's low pressure chamber. The influence of rotational speed, gas composition, rotor geometry and flap presence in the wake is evaluated on thrust and torque measurements. The paper concludes on the feasibility of a Martian MAV, proposes a concept of drone directionally controlled by flaps, and gives some perspectives for future investigations.

MARTIAN ATMOSPHERE AND AERODYNAMIC CONDITIONS

The main challenge faced in the Martian atmosphere, in terms of flight capability, is the extreme low density: about eighty times lower than on Earth. During daytime, it can fluctuate between 0.014 and 0.020 kg/m^3 (Millour, Ref. 19). Table 1 compares the average characteristics of Earth's and Mars' atmospheres. Martian equivalent conditions can be found on Earth in the stratosphere at an altitude of about 30 km. One can easily imagine that flying a VTOL MAV at such an altitude on Earth is very challenging. Martian

atmospheric temperature, strongly controlled by suspended dust holding solar radiations, is also lower than on Earth and eminently variable with 60 °C of diurnal near-surface range (Leovy, Ref. 20). Low temperature combined with low specific heat ratio (Martian atmosphere is composed of 96% of carbon dioxide CO_2) directly lowers the speed of sound. This gives a compressible aspect of the flow around the blades, especially for small helicopter designs because high rotational speed is needed. Despite these challenges, the low Martian gravity (about two and a half times lower than on Earth) eases flight compared to Earth's stratosphere. The viscosities are quite comparable between Mars and Earth, which means that the low Reynolds numbers come mainly from the low density. It is worth noting that the Martian atmosphere is very turbulent, with strong winds and dust storms. This is a key point to take into account when designing for stability and operability of a Martian MAV.

Table 1: Average characteristics of Earth's and Mars' atmospheres.

Quantity	Earth (ground)	Mars (ground)	Earth (30 km)
Gravity (m/s^2)	9.81	3.72	9.78
Density (kg/m^3)	1.225	0.0167	0.0177
Temperature (°C)	15	-63	-46
Pressure (Pa)	10^5	660	1150
Dynamic viscosity (Pa.s)	$1.8\ 10^{-5}$	$1.06\ 10^{-5}$	$1.47\ 10^{-5}$
Sound velocity (m/s)	340	230	300
Specific heat ratio	1.4	1.32	1.4
Gas constant (J/kg/K)	287	188	287

Because of the very low density and the small size of the vehicle, one may rightly question about the continuum aspect of the flow around the blades. This point can be addressed through the Knudsen number, which can be expressed as:

$$Kn = \frac{M}{Re}\sqrt{\frac{\gamma\pi}{2}}$$

Even for a transonic flow at $M = 0.7$ and ultra-low Reynolds number of 1000, Knudsen number is equal to 0.001, which is far below the 0.1 value considered as the limit for continuum physics. This means that traditional aerodynamics based on Navier-Stokes equations applies.

As mentioned above, the diameter of the MAV rotating propulsion system considered here is 30 cm. Simulations are performed in Martian conditions with the daytime minimal value of the density (0.014 kg/m^3) and the average value of the speed of sound (230 m/s). A parametric investigation made previously by Bézard (Ref. 21) shows that the mass lift by an isolated hovering rotor lies between 100 g and 300 g only, taking into account the limit of 0.7 for the maximum tip Mach number (obtained at a rotational speed of 10,000 rpm) to avoid strong transonic phenomena on the blades and consequent power penalty due to shock waves. In Martian gravity, the corresponding thrust lies between 0.37 N and 1.1 N. For chord values lower than 10 cm, Reynolds numbers are below 10,000. To know whether the boundary layer over airfoils is laminar or turbulent, linear stability analyses were performed on different airfoils at $Re = 6{,}000$ and $M = 0.5$ (Désert, Ref. 22). The calculated N factor (e^N method) is always below 1, proving a fully laminar flow. A concordant result is presented in the stability analysis section.

VALIDATION OF UNSTEADY LAMINAR NAVIER-STOKES SIMULATIONS

As mentioned previously, the flow around the blades is laminar for $Re < 10{,}000$. It is also known that laminar boundary layer separation easily occurs on cambered airfoils, even at moderate angle of attack, and evolves rapidly into unsteady flow. Unsteady laminar Navier-Stokes solver seems to be the best method to evaluate airfoils and blades in Martian conditions. Simulating both laminar and compressible flow around geometries is however unusual and the solver needs to be validated before. The ONERA's Navier-Stokes code named *elsA* (Cambier, Ref. 23) is used here. It is based on an integral form of the compressible Navier-Stokes equations. Simulations performed on a same test case with another Navier-Stokes code (*STAR-CCM+*) give comparable results for both codes (Désert, Ref. 24).

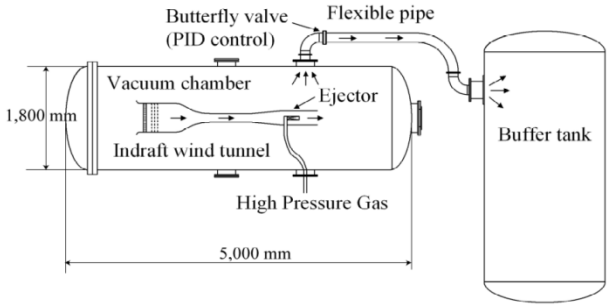

Figure 1. Sketch of the Mars Wind Tunnel facility at the University of Tohoku.

The *Mars Wind Tunnel* (MWT), located at the University of Tohoku, is a depressurized facility reaching Martian density for different Mach numbers (Figure 1). For validation purpose, the triangular airfoil is considered (Munday, Ref. 16). The leading edge camber and sharpness causes significant unsteadiness in the flow, making it interesting for numerical validation. MWT's experiment is supposed to recreate 2D flows. However, pressure sensitive paint (PSP) measurements show the three-dimensionality of the flow over the airfoil caused by the influence of the side walls of the test section. Therefore, the test section is fully simulated and structured 3D grids are created around the airfoil, including all the walls of the wind tunnel (Figure 2). Three angles of attack are considered for the simulations: 5°, 10° and 15°. 2D H-grids are first created with 180 cells mapping the airfoil's upper surface and 100 for the lower surface. 3D grids are generated from 2D grids with 130 cells in the spanwise direction for a width of 3.3 chords, with a total of 15 million cells. Grid convergence was verified for each Navier-Stokes simulation.

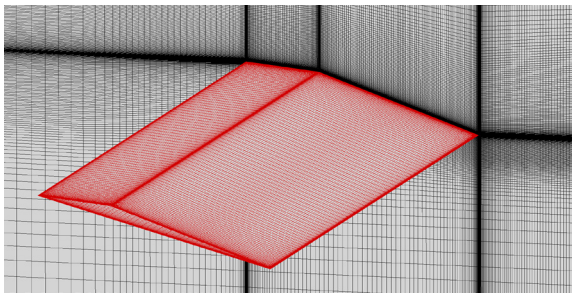

Figure 2. Triangular airfoil. Surface grid

The present 3D numerical simulations corroborate the three-dimensionality of the flow in the facility, as seen in Figure 3 that plots iso-surfaces of Q-criterion for $Re = 3000$, $M = 0.5$ and $\alpha = 10°$. Unsteady laminar Navier-Stokes solver perfectly predicts the 3D lift and drag coefficients generated at the two first angles of attack (5° and 10°) as shown in Figure 4. At $\alpha = 15°$, corresponding to a fully detached flow, the computed lift is slightly over-estimated. The complex physics of fully detached flow is not properly simulated because of low mesh density away from the airfoil slice. However, in the present investigation, airfoil aerodynamic performance is compared in the most effective range of angles of attack, i.e. when the flow is not fully separated. Therefore, the solver is validated for the simulation of not fully separated 3D flows and should also provide reliable 2D predictions.

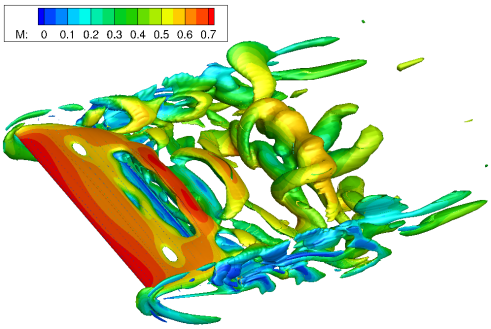

Figure 3. Triangular airfoil. Q-criterion colored by Mach number at $Re = 3000$, $M = 0.5$, $\alpha = 10°$.

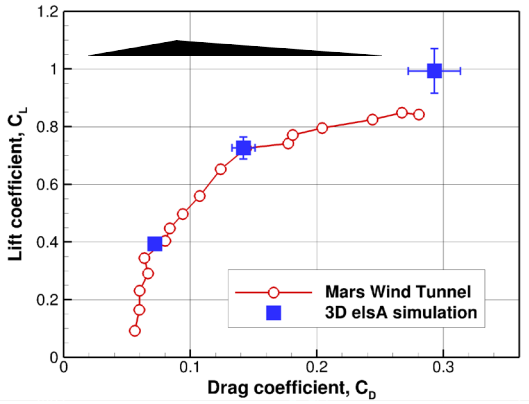

Figure 4. Triangular airfoil. Lift and drag coefficients at $Re = 3000$, $M = 0.5$.

AIRFOIL OPTIMIZATION

A complete rotor shape could be directly optimized by 3D Navier-Stokes simulations. However, the number of parameters describing the geometry can be very important and would involve a great computational and meshing effort. It was decided to split the rotor design into firstly, the airfoil design (camber and thickness distributions) and secondly, the blade design (chord and twist distributions). Again, designing the airfoil is possible by Navier-Stokes simulations. For the same reason, a simpler aerodynamic evaluation based on XFoil (Drela, Ref. 8) is used. XFoil is a 2D high order panel method fully coupled with an integral boundary layer method. Compressibility is taken into account through Kármán-Tsien corrections. This tool was compared with *elsA* Navier-Stokes code by Désert (Ref. 25) and it was shown that for the most performant aerodynamic conditions, that is non-fully separated flow, both codes give comparable thrust and drag coefficients for 10^8 times lower computational effort with Xfoil. Xfoil still compares well with unsteady Navier-Stokes simulations for higher angles of attack where limited trailing edge flow separation occurs, but it is no more in agreement when the unsteadiness of the flow is important, e.g. when fully separated flow occurs. In these conditions, the unsteady laminar Navier-Stokes simulations, which were proven previously to be the most relevant, provide much higher lift than Xfoil.

In a purpose of optimization, automatic airfoil generation with finite parameters is essential. The parameterization method based on Class-Shape function Transformation (Ref. 26) was chosen for its ability to recreate any C^2 continuous airfoil shapes with a restricted number of parameters. Five parameters are used to reflect the shape of the camber or the thickness distribution. The objective of the optimization is to produce maximum lift with minimum drag, which is equivalent to maximizing the lift-to-drag ratio C_L/C_D. But the objective can also be maximizing $C_L^{3/2}/C_D$, which is linked to the range of an aircraft. The best is to combine both in a unique objective function. Because aerodynamic conditions are not accurately known and for sharp design avoidance, the optimized airfoil is evaluated to be efficient over a large range of Reynolds number and angles of attack. The final objective function is thus an average of the sum $C_L/C_D + C_L^{3/2}/C_D$ over four angles of attack around the optimum, and an average over three Reynolds numbers: 2000, 6000 and 10,000. The optimization process consists in evaluating the entire parameter domain with an increasing proximity between the different sets of parameters. This demands a very important number of set evaluations. Approximately half a million XFoil evaluations are carried out for one optimization. Different optimizations are performed, from incompressible to compressible, from thickness and camber separate optimizations to both camber and thickness optimization. Finally, the optimized airfoil for thickness and camber at $M = 0.5$ is kept for the rotor design.

The corresponding camber and thickness distributions are displayed in Figure 5. The geometry is close to the one

obtained by Kunz (Ref. 5). The high camber at leading edge ($x/c = 0$) allows the flow to be adapted at high angles of attack: it limits acceleration and prevents leading edge separation. The high camber at trailing edge ($x/c = 1$) limits the extent of the boundary layer separation and the pressure drag penalty. The maximum camber is around 6% chord. The thickness is very low and almost constant, about 2% chord. It is a common feature of airfoils at very low Reynolds numbers. Surprisingly the trailing edge is rounded and not sharp, contrarily to classical airfoils. This rounded trailing edge slightly reduces the adverse pressure gradient on the upper side and limits separation, with little base drag penalty because the laminar flow is already separated over about 20% chord.

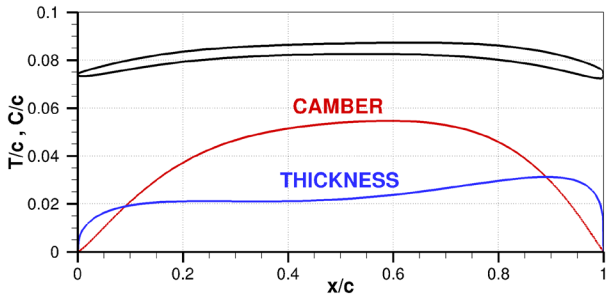

Figure 5. Geometry of optimized airfoil.

2D NAVIER-STOKES SIMULATIONS

Optimized airfoil around the design point

In order to show the main features of compressible and ultra-low Reynolds number's flows, the optimized airfoil was simulated around the design point with *elsA* Navier-Stokes code. Unsteady laminar simulations are performed. Figure 6 shows the instantaneous flow at $Re = 6000$, $M = 0.5$, for an angle of attack $\alpha = 5°$ where the flow is attached on most of the chord (Figure 6a), and $\alpha = 8°$ where the flow is fully separated (Figure 6b). Note that large boundary layer thickness is caused by the ultra-low Reynolds number. At the design operating point $\alpha = 5°$, a flow separation occurs close to the trailing edge at about 85% chord and classical Kármán vortex instabilities form downstream in the wake. As said previously, the camber in the trailing edge region shifts this laminar separation downwards. At $\alpha = 8°$, even if the flow is separated, the mean lift coefficient is still high ($C_{Lmean} = 1.45$) compared to its value at $\alpha = 5°$ ($C_{Lmean} = 0.95$) where the flow is attached. This behavior comes from vortices periodically forming at the leading edge and rolling close to the upper surface before leaving the airfoil, thus producing high local velocities (up to local Mach number of 0.8) and low local pressures, explaining the over-production of lift on the upper side.

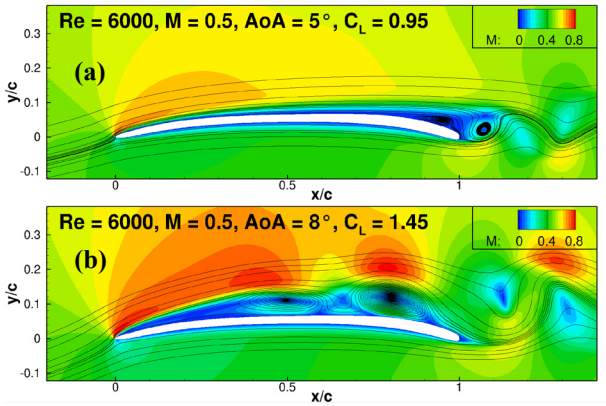

Figure 6. Instantaneous Mach number contours at $Re = 6000$ and $M = 0.5$. (a) $\alpha = 5°$, (b) $\alpha = 8°$

Comparison with other airfoils

It is interesting to compare the optimized airfoil to other ones already known in the literature as performant at ultra-low Reynolds numbers. First, Bohorquez (Ref. 7) investigated the influence of camber on simple plates of constant thickness (2.5% and 3.75% chord) and showed that a plate cambered at 6% chord is optimal in terms of maximum lift-to-drag ratio at Reynolds numbers between 15,000 and 60,000. Such an airfoil is thus considered for comparison. Secondly, by biomimetic considerations, it is argued that insect wing sections are particularly well adapted to ultra-low Reynolds number flows. Kesel (Ref. 27) measured the performance of dragonfly's wing sections at a Reynolds number of 10,000. These sections have already been investigated in the literature. The dragonfly's outer wing section at 70% span is retained here for comparison. Both airfoils are generated with a constant thickness of 2% chord to be compared to the optimized airfoil.

The instantaneous flows on both airfoils at $Re = 6000$, $M = 0.5$ and $\alpha = 5°$ are presented in Figure 7. They can be compared to the flow over the optimized airfoil presented previously in Figure 6. The cambered plate is very close to the optimized airfoil: the flow is attached on most of the upper side and separates in the trailing edge region, except that the separation occurs upper on the cambered plate compared to the optimized airfoil, at 65% chord. The mean lift coefficients are very close for both airfoils (0.95 and 0.93), but drag is higher for the cambered plate because of the larger separation. For the highly corrugated dragonfly's section, separations occur at different locations on the geometry, on both sides, resulting in a lower lift coefficient (0.76) and a much higher drag. This is illustrated in Figure 8 which shows the lift-to-drag ratio versus the lift coefficient for the three airfoils at $Re = 6000$ and $M = 0.5$. The cambered plate and the optimized airfoil are again very close, but the optimized airfoil has the better performance with a maximum C_L/C_D value of 12.5 obtained at $C_L = 1$. The dragonfly wing section shows poor performance with a maximum C_L/C_D value of 9 obtained at $C_L = 0.7$. This is due to large separated regions at high angles of attack, as seen

previously. Such corrugated airfoils are proved to be performant for flapping wings, but not for rotor applications, especially in hover. Smooth, thin and highly cambered geometries are better suited.

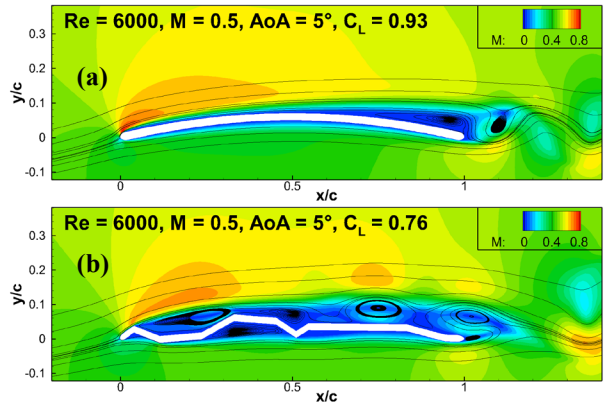

Figure 7. Instantaneous Mach number contours at $Re = 6000$ $M = 0.5$ $\alpha = 5°$. (a) 6% cambered plate, (b) dragonfly wing section.

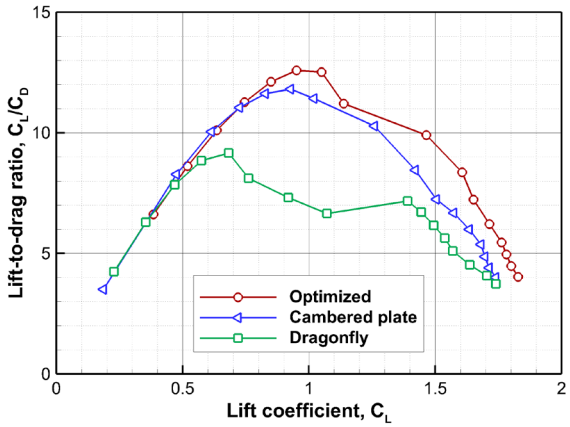

Figure 8. Lift-to-drag ratio for different airfoils at $Re = 6000$ and $M = 0.5$.

Stability analysis

It was previously assumed that the flow over airfoils was laminar for Reynolds number below 10^4, based on previous research. A linear stability investigation (e^N method) was performed for the optimized airfoil at different conditions to confirm this assumption. For the case presented here, boundary layer quantities on the upper side of the airfoil were extracted from the flow presented in Figure 6 at $Re = 6000$, $M = 0.5$, $\alpha = 5°$. The physical quantities (velocity, pressure, temperature, viscosity) were obtained considering the Martian conditions presented in Table 1. The result of the stability analysis is presented in Figure 9 which shows the chord evolution of the N factor for the most unstable mode frequencies. The computations are stopped at the separation location, at about 85% chord. The most unstable mode occurs at a frequency of about 230 Hz, which is much lower than for classical unstable modes in boundary layers at high Reynolds numbers. The envelope curve (black line) shows that the maximum N factor value is 0.3, far below the value for which transition could occur, which is around 9 in flight conditions at low turbulence levels on Earth. Computations performed in other conditions (not shown here) provided maximum N factor values always below 1. This stability analysis tends to prove that the flow remains laminar over 2D rotor blade sections of MAV on Mars.

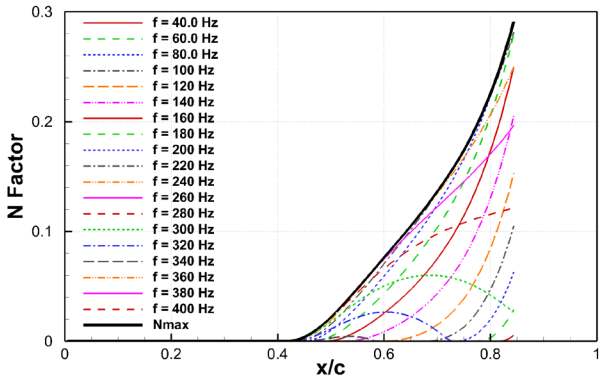

Figure 9. N factor evolution for the optimized airfoil at $Re = 6000$, $M = 0.5$, $\alpha = 5°$.

Optimized airfoil at different conditions

Unsteady laminar Navier Stokes simulations with *elsA* code are extensively performed over a large range of Reynolds numbers, Mach numbers and angles of attack to provide the necessary data base for the rotor optimization. Figure 10 to Figure 12 show the effect, on the flow and on the aerodynamic coefficients, of the Reynolds number at a given Mach number of 0.5. The lift coefficient and the lift-to-drag ratio are strongly dependent on the Reynolds number (Figure 11 and Figure 12). At $Re = 10{,}000$, the maximum lift-to-drag ratio is achieved with a value of 15, which is relatively small compared to more than 100 for classical airfoils at high Reynolds number. The minimal value of C_L/C_D is encountered at $Re = 1000$ with a value of 5 because boundary layers are very thick, as seen on the corresponding flow in Figure 10. For every evaluated Reynolds number, the lift coefficient of maximum performance is close to 1. The break in the evolution of the efforts with the increasing angle of attack, visible for $C_L > 1$ and for Re values greater than 3000, is due to the occurrence of highly unsteady separated flow, as seen previously in Figure 6. At these very low Reynolds numbers, the lift coefficient still increases at high angles of attack and no stall occurs. A C_L of 2 is almost reached at 15° angle of attack for the highest Reynolds number values.

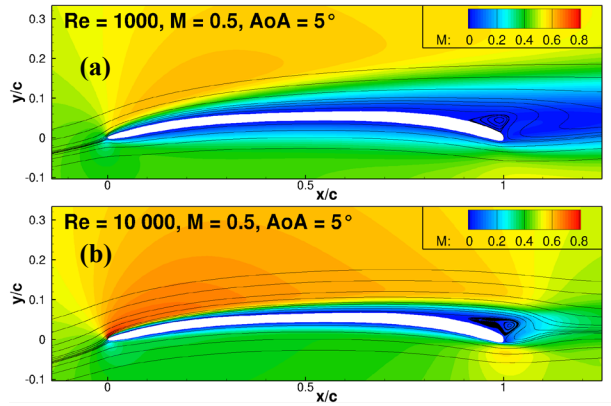

Figure 10. Mean Mach number contours at $M = 0.5$ and $\alpha = 5°$. (a) $Re = 1000$, (b) $Re = 10{,}000$.

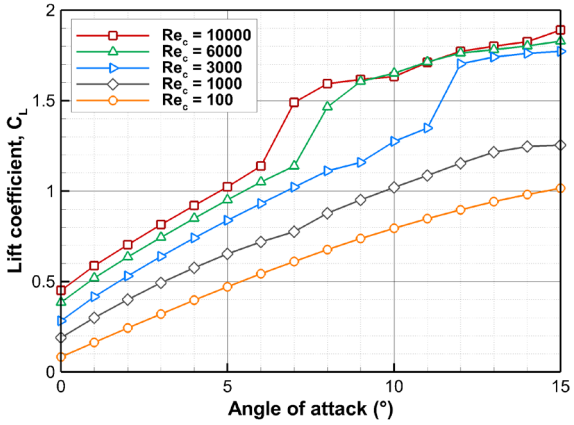

Figure 11. Effect of Reynolds number on mean lift coefficient. $M = 0.5$.

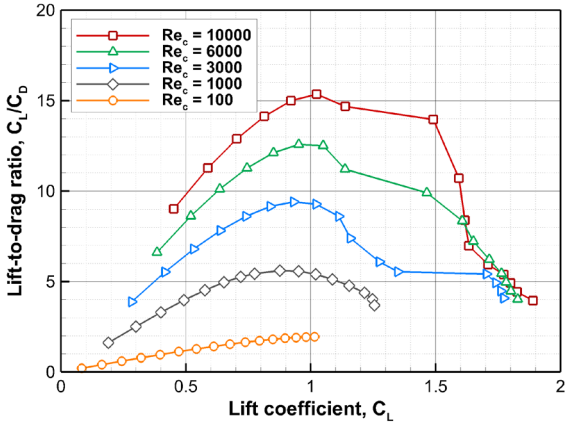

Figure 12. Effect of Reynolds number on mean lift-to-drag ratio. $M = 0.5$.

Figure 13 to Figure 15 show the effect of the Mach number at a given Reynolds number of 3000. The C_L increases with the Mach number (Figure 14), except at $M = 0.9$ where a large separation occurs (not shown here). The C_L/C_D is almost independent of the Mach number up to $M = 0.7$ (Figure 15). For $M > 0.7$, the performance decreases rapidly with the Mach number, due to the occurrence of supersonic regions and shock waves, as seen on the corresponding flow at $M = 0.8$ (Figure 13). $M = 0.7$ is the divergence drag Mach number and should be considered as a limit for the blade tip Mach number, which gives a maximal rotational speed of about 10,000 rpm in Martian conditions for a rotor of 30 cm of diameter.

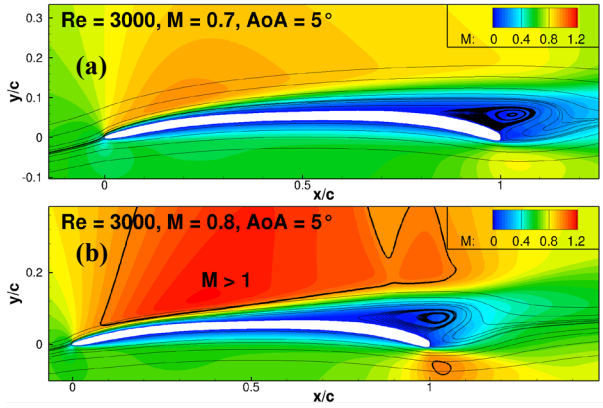

Figure 13. Mean Mach number contours at $Re = 3000$ and $\alpha = 5°$. (a) $M = 0.7$, (b) $M = 0.8$.

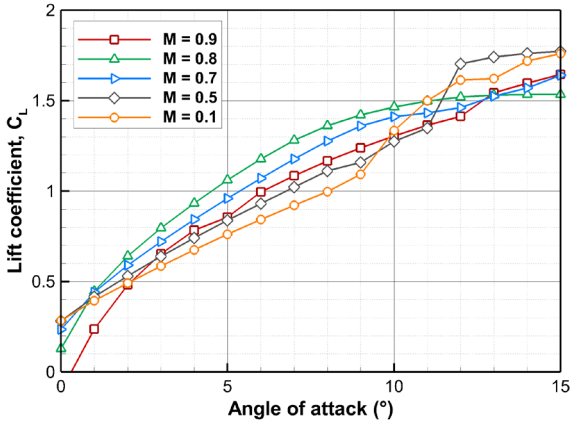

Figure 14. Effect of Mach number on mean lift coefficient. $Re = 3000$.

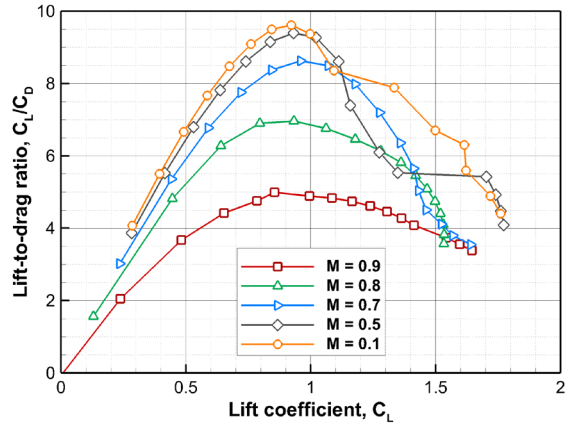

Figure 15. Effect of Mach number on mean lift-to-drag ratio. $Re = 3000$.

EVALUATION OF SIMPLER NUMERICAL SOLVERS FOR PERFORMANCE EVALUATION OF ROTORS IN HOVER

As already discussed before, using 3D unsteady Navier-Stokes simulations for rotor optimization is time consuming and simpler methods are preferred, on the condition that they simulate accurately enough the physical behavior of the flow for an optimization process. Two low-computational cost solvers are evaluated here: one based on the Blade Element Momentum Theory (BEMT), named QMIL/QPROP developed by Drela (Ref. 28), the second based on the Free Vortex Method (FVM) named PUMA, and developed by ONERA (Le Bouar, Ref. 29), which combines a lifting line approach and a free wake model. Both methods rely on airfoil aerodynamic characteristics given here by 2D unsteady laminar Navier-Stokes simulations. A three-bladed rotor was designed using BEMT (QMIL) by minimizing induced loss. The chords are modified in the root region to avoid overlapping of blades at the hub, in order to help manufacturing the rotor. The rotor has a solidity σ of about 0.23. The planform of one blade is visible in Figure 17. Numerical evaluations are performed on the BEMT optimized rotor. For Navier-Stokes simulations, only a third of the domain is simulated with periodic conditions (sides 1 and 2, Figure 16) for blade-to-blade interactions. For convergence facilitation, a velocity field based on Froude's theory is implemented through upper and lower domain boundaries (sides 3 and 4, Figure 16). A 4 cm diameter hub is added to the rotor and extended to the exit with slip conditions on it. A fully structured grid of about 12 million cells is generated and a view of the blade surface grid is presented in Figure 17.

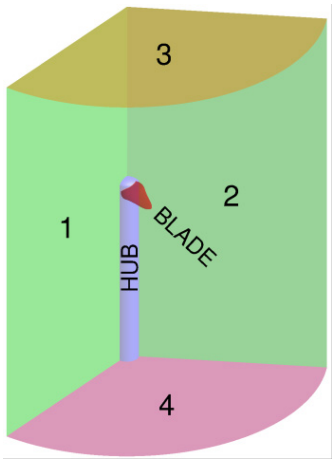

Figure 16. Computational domain.

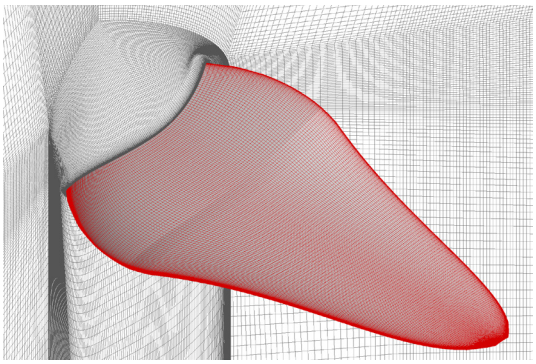

Figure 17. BEMT optimized rotor. Surface grid.

The local lift coefficient distributions along the span are compared in Figure 18, for a rotational speed of 7500 rpm and a total thrust of 0.37 N (100 g in Martian gravity) evaluated by BEMT theory. The Martian density was set to 0.014 kg/m^3, which is the lowest value encountered in daytime on Mars. FVM and Navier-Stokes estimations of local C_L are close, which is not the case for BEMT results. The main difference between FVM and BEMT is the modeling of the wake. The PUMA free wake model allows a better estimation of the local induced angles, as in Navier-Stokes simulations. In terms of computational cost, BEMT simulations are almost instantaneous ($\sim 10^{-5}$ h). FVM simulations take more time to converge ($\sim 10^{-2}$ h per processor), which is however five orders of magnitude lower than the computational cost of Navier-Stokes simulations ($\sim 10^{3}$ h per processor). Therefore, FVM provides accurate results for acceptable computational time and is thus adequate for rotor optimization.

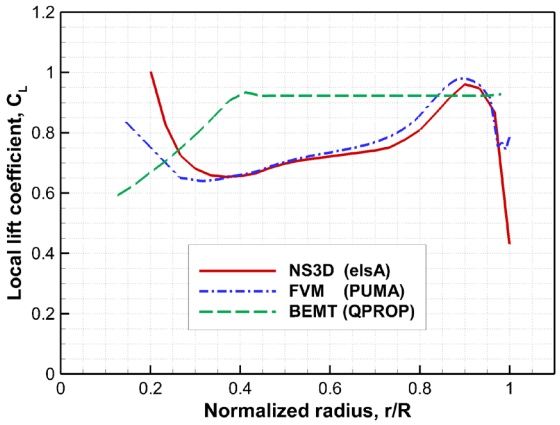

Figure 18. BEMT optimized rotor. Local lift coefficient distributions vs. span location at 7500 rpm.

ISOLATED AND COAXIAL ROTOR OPTIMIZATION BASED ON FVM SIMULATIONS

Method

Theoretically optimal rotor blades have nearly equal Reynolds number distributions along the span, compensating

local speed variation with chord length. Therefore, in a non-constrained optimization process, chord length tends to infinity at the root of the blade. In order to optimize a realizable rotor shape, blade root distribution has to be constrained. A no-overlapping condition is not sufficient since optimized twist at root tends to a large value and the shape of the rotor tends to be non-feasible and non-optimal in terms of mass. For manufacturing feasibility and structural robustness, twist at root is set to zero. The corresponding length of the chord is calculated in agreement with the no-overlapping constraint. Since most of rotor thrust is generated by the blade tip area, constrained chord and twist distributions at root allow restricting the weight of the rotor in the most inefficient part of the blade. Rotors are made of three blades, an odd number, in order to avoid specific vibration axes. In a purpose of optimization, automatic generation of the shape with finite parameters is essential. Spline representation with five control points is used to generate the shape of chord or twist distributions. The optimization process consists in evaluating the entire domain of the ten parameters with an increasing proximity between the different sets of parameters, as in the 2D optimization.

The present investigation aims at building a propulsion system able to sustain a given mass in hover on Mars. Two objectives are considered: 200 g (thrust $T = 0.74$ N) and 600 g (thrust $T = 2.23$ N). First step is to optimize a single rotor generating a thrust of 100 g ($T = 0.37$ N) or 300 g ($T = 1.11$ N). Then, for coaxial configuration optimization, the optimized single rotor is used as the upper rotor without modification. Only the lower rotor is optimized for generating the remaining 100 g or 300 g of thrust, if possible, while cancelling the residual torque of the coaxial propulsion system at the same rotational speed. It is possible to release the constraint on the rotational speed of the lower rotor, to allow a faster rotation and smaller chords, and thus lower mass. However, it could induce earlier transonic phenomena and lower performance. It could also induce some drawbacks on the motor and the control systems. Same torque and rotational speed on both rotors means same power. It allows both motors to be fully identical. This solution seems to be preferable for a demonstrator, but there is no strong argument at this point to confirm this choice. The influence of induced velocity and vorticity coming from the upper rotor is taken into account thanks to the free wake model. The lower rotor is assumed to have little impact on the upper rotor. Spacing between coaxial rotors is set to $h = 0.08$ m ($h/R \sim 0.5$). For $h/R > 0.4$, it has been shown that the spacing has little impact on global performance (see Bohorquez, Ref. 7, and Lakshminarayan, Ref. 11). In the optimization process based on FVM, the rotational speed corresponding to a given thrust is obtained from three solver evaluations at different rotating speeds. Values are interpolated assuming that thrust and torque are functions of Ω^2. More than 30,000 isolated upper rotor and 6000 lower rotor geometries were evaluated with the FVM solver.

Optimized geometries

The optimized three-bladed upper and lower rotors exhibiting the lowest power consumption for a 200 g total thrust on Mars are presented in Figure 19 and Figure 20 respectively, and for a 600 g total thrust in Figure 21 and Figure 22. Twist values at the control points of the splines are also indicated. The upper and lower rotors rotate at 6100 rpm for the 200 g configuration and 9600 rpm for the 600 g configuration. The optimized shapes of the upper rotors are highly twisted and elliptic, with very large chords. Their solidity σ is respectively 0.32 and 0.35 for the 200 g and 600 g configurations. These shapes are quite unusual and far from the classical propellers for terrestrial drones. Contrarily, the shape of the lower rotor is slimmer in the central section of the blade and is larger in the outer part. Upper and lower twist distributions are close. Note that for all rotors, the optimization based on FVM tends to a low twist at blade tip ($\beta = 2°$ to $7°$) for tip vortices and induced drag reduction. Both coaxial geometries are close, the chords and twist are slightly higher for the most loaded one (600 g). They differ mostly by their operating rotational speed.

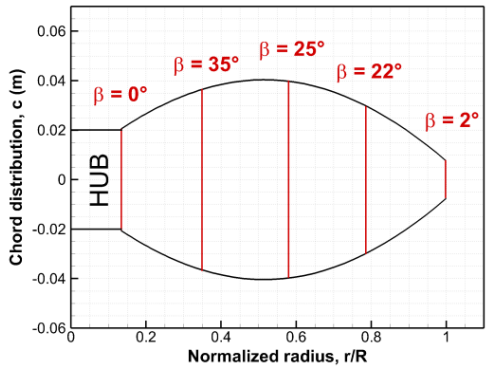

Figure 19. Optimized coaxial configuration for 200 g total thrust on Mars. Upper rotor shape.

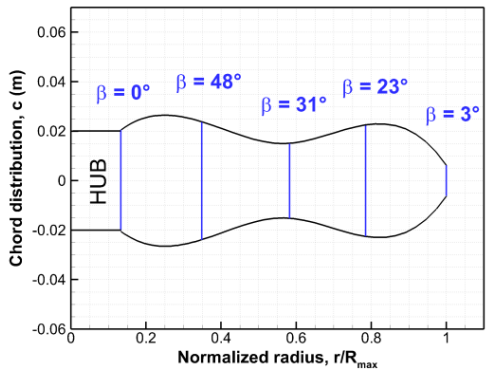

Figure 20. Optimized coaxial configuration for 200 g total thrust on Mars. Lower rotor shape.

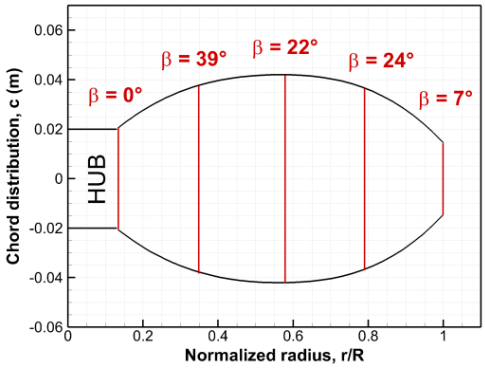

Figure 21. Optimized coaxial configuration for 600 g total thrust on Mars. Upper rotor shape.

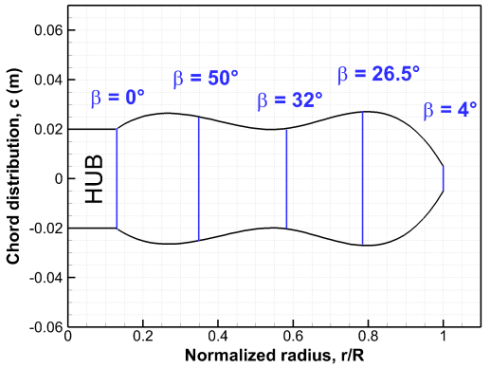

Figure 22. Optimized coaxial configuration for 600 g total thrust on Mars. Lower rotor shape.

Local loads

The local thrust distributions along the span evaluated by the FVM solver for the 200 g and 600 g coaxial rotors are presented in Figure 23 and Figure 24 respectively. The thrust distribution on the upper rotors is rather usual. Approaching the tip, because of the reduced twist of the geometries, the local thrust is quickly reduced, which limits the strength of the tip vortex and the consequent induced drag penalty. The maximum local thrust is located at about 80% span. On the lower rotors, the evolution is quite different: the thrust is flattened in the central part of the blade. It corresponds to the part of the geometry where the chords are smaller and the twist is reduced. It is not so clear why the optimization process provides such geometries and such a local thrust evolution. But it is obviously linked to the upper wake interaction. Because of the wake contraction, the outer part of the lower blade ($r/R > 0.7$) evolves in a non-disturbed flow. The optimization process took advantage to this flow feature by increasing the chords and the loads in this region. In the central part, the interaction with the upper wake interaction is strong, and the inflow velocities are much more important. The chords and the local loads are then reduced. The local thrust distributions of the upper and lower blades have a similar comparison for the 200 g and 600 g coaxial propulsion systems.

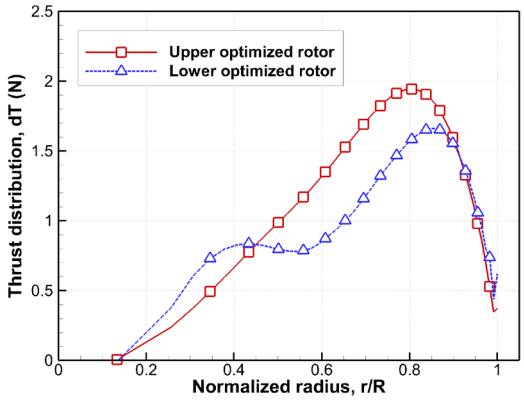

Figure 23. 200 g optimized coaxial configuration. Local thrust spanwise distributions at 6100 rpm.

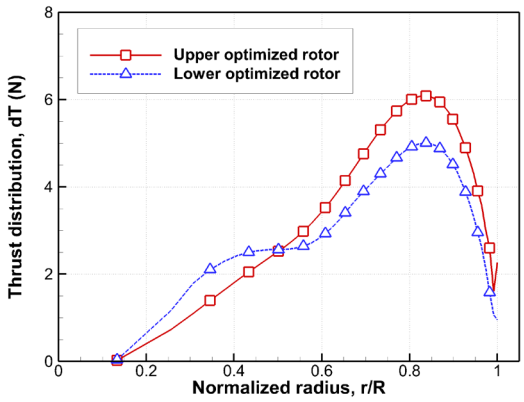

Figure 24. 600 g optimized coaxial configuration. Local thrust spanwise distributions at 9600 rpm.

The solidity and the thrust and power coefficients evaluated by FVM are presented in Table 2 for all the optimized rotors. The BEMT optimized rotor shows a low C_T, indicating poor thrust performance. C_P is also low, which means that C_T/C_P is comparable to FVM optimized rotors (about 4.3). A better performance indicator for rotor comparison is the power-loading T/P, which indicates the power consumption for a given lifted mass. It can be shown that:

$$\frac{T}{P} = \frac{C_T}{C_P} \times \frac{1}{\Omega R}$$

which means that it includes the minimization of the rotating speed in the performance indicator. The rotating speed for generating 100 g of thrust is higher for the BEMT optimized rotor compared to the FVM optimized rotor. The calculated power-loading value at the design rotational speed is about 0.037 N/W.

The FVM optimized rotor for 100 g thrust (upper rotor of the 200 g thrust coaxial configuration) has a much higher C_T. Part of it comes from a higher solidity, the other part comes from a chord and twist optimization with more physics involved in the process. It can be shown that the blade-loading coefficient C_T/σ is better for the FVM rotor (0.13) than for the BEMT rotor (0.11). C_T/C_P is lower for the FVM

rotor (3.6), but because of a lower rotational speed of 6100 rpm, the power-loading T/P is about 0.038 N/W, which is better than for the BEMT rotor. The lower rotor of the corresponding coaxial configuration generates a lower C_T, which means that the thrust capability is reduced by 20% because of the upper wake interaction and the zero total torque and equal rotational speed constraints. This result was expected from the spanwise thrust distributions presented in Figure 23.

For the 600 g total thrust coaxial configuration, the upper rotor has the highest solidity and C_T values. The blade-loading coefficient C_T/σ is also high (0.14). Of course, because of the higher rotational speed than for the previous coaxial configuration, the power-loading is lower than the 200 g coaxial configuration, about 0.023. C_T/C_P is about 3.4 for the upper rotor, which is less than for the 100 g optimized FVM rotor. The lower rotor has 17% less thrust capability than the upper rotor, which was again expected from the spanwise thrust distributions, presented in Figure 24.

The Figure of Merit can be calculated from C_T and C_P values of Table 2. It is an indicator of rotor efficiency. Usual values for terrestrial drones or helicopters in hover are around 0.7 for aerodynamically performant ones. Here, the calculated values of Figure of Merit are between 0.51 and 0.54 for the FVM optimized upper rotors, which is low, but acceptable considering the ultra-low Reynolds number flow conditions providing a great amount of viscous drag.

Table 2: Thrust and torque coefficients of the optimized rotors. FVM computations.

Optimized rotor	Solidity σ	C_T	C_P
BEMT (100 g thrust)	0.23	0.025	0.0058
FVM upper (100 g thrust)	0.32	0.041	0.011
FVM lower (100 g thrust)	0.21	0.033	0.011
FVM upper (300 g thrust)	0.35	0.049	0.014
FVM lower (300 g thrust)	0.23	0.041	0.014

3D NAVIER-STOKES EVALUATION

Isolated rotors

The isolated rotors were evaluated with two Navier-Stokes codes: *elsA* and *STAR-CCM+*. Simulated pressure distributions were very close (Désert, Ref. 24) and only the loads evaluated by *elsA* are presented here. The structured meshing follows the same procedure as presented previously. Only a third of the domain is meshed, with periodic boundaries (see Figure 16). The domain contains about 12 million cells. The hub extends as a plain cylinder below the rotor. The computational time step is 10^{-5} s, corresponding to 0.4° rotor rotation. The Gear scheme is used with 10 sub-iterations. About 15 full rotations are performed, which is enough to obtain a stabilized solution.

Surface pressure (difference from ambient pressure), frictions lines and iso-surfaces of Q-criterion are presented in Figure 25 for the BEMT optimized rotor and in Figure 26 for the FVM optimized rotor (both for 100 g thrust on Mars). On the BEMT rotor, the boundary layer flow becomes three-dimensional approaching the trailing edge where separation occurs, as for the 2D airfoil flow. A 3D separation occurs close to the tip from 90% span, leading to a strong tip vortex, as shown by the Q-criterion display, generating high lift coefficients, as already noticed in Figure 18. The tip vortex is intense because the pressure difference and the spanwise pressure gradient are large at the tip. It is the reason why the vortex does not dissipate rapidly. Some flow instabilities are visible downstream the outer part of the blade, at the trailing edge of the section. They are caused by the laminar boundary layer separation that forms instabilities in the wake as seen in 2D. These instabilities could probably cause vibrations on the blade. However, the time evolution of the thrust shows fluctuations of only ±2%, indicating that the unsteady blade pressure distribution is weakly influenced by this effect.

On the FVM optimized rotor, the curvature of the friction lines shows that the boundary layer flow is strongly three-dimensional. No more separation occurs at trailing edge. The shape of the friction lines at the leading edge indicates a 3D-separated region: a stable leading edge vortex (LEV) occurs and leaves the surface close to the tip, as seen on the Q-criterion. This phenomenon is enhanced by the low Reynolds numbers and the low aspect ratio of the blade. This LEV was not expected as the FVM solver is not able to reproduce this phenomenon, but it seems to have little impact on the performance. The pressure difference and the spanwise pressure gradient at the tip are lower than for the BEMT optimized rotor, because blade twist is lower in this region, minimizing the loads and the induced loss. It leads to a weaker tip vortex, which oscillates and dissipates rapidly in the wake. Another vortex is visible in the wake. As mentioned previously, it comes from the LEV and leaves the blade at about 85% span. This vortex induces a low pressure region on the blade surface, visible in Figure 26. The tip vortex and the LEV rotate around each other before merging and dissipating rapidly.

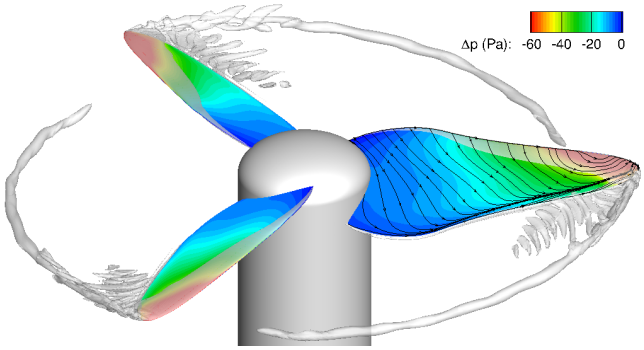

Figure 25. BEMT optimized rotor. Surface pressure, friction lines and iso-surfaces of Q-criterion.

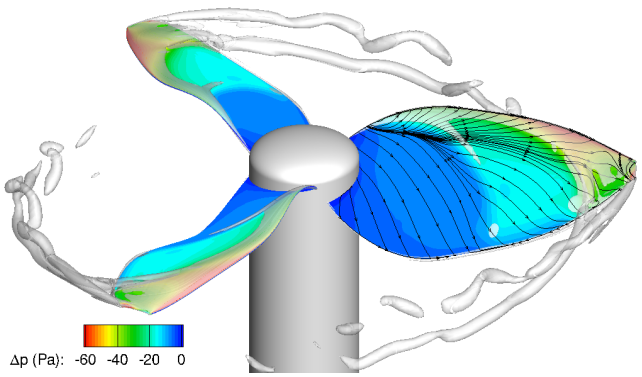

Figure 26. FVM optimized rotor. Surface pressure, friction lines and iso-surfaces of Q-criterion.

Effect of compressibility

The FVM optimized rotors rotate at 6100 rpm, generating 100 g of thrust, and at 9600 rpm for 300 g of thrust, corresponding respectively to tip Mach numbers of 0.42 and 0.66 in Martian conditions. These values are below the airfoil transonic divergence estimated previously to 0.7. As for the airfoil, it is interesting to investigate the effect of the compressibility on the rotor loads by increasing the rotational speed up to transonic regime. Navier-Stokes simulations were performed on the 100 g thrust FVM optimized upper rotor only, from 5000 rpm to 16,000 rpm, which gives M_{tip} values from 0.35 to 1.15 in Martian conditions.

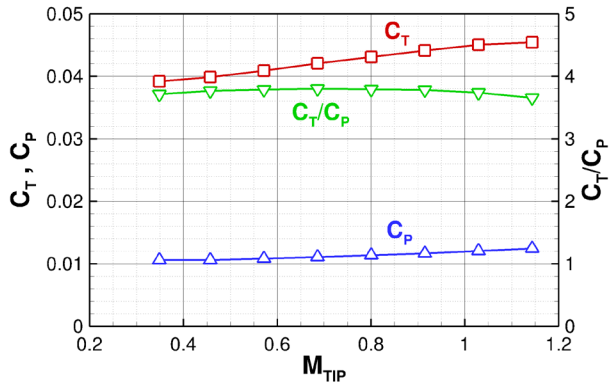

Figure 27. C_T and C_P evolution with M_{tip}. FVM optimized upper rotor (100 g thrust). *elsA* simulations.

The evolutions of the thrust and power coefficients and of the C_T/C_P ratio are presented in Figure 27. C_T and C_P increase continuously with the tip Mach number, which is a physical consequence of the compressibility. C_T seems to reach a plateau for tip supersonic flow. One expected the power coefficient to rise quickly in transonic and supersonic regime because of the local drag divergence but no power divergence is observed. C_T/C_P is almost constant. It reaches a maximum value around $M_{tip} = 0.7$, and decreases regularly for greater values. Close inspection of the corresponding flow fields (not presented here) reveals very weak local shock waves because of the strongly three-dimensional flow and the very thick boundary layers, tending to spread away the compression waves.

Coaxial rotors

Coaxial rotor computations were performed with *STAR-CCM+* code because of its simpler implementation and unstructured meshing tool. The grid is composed of 28 million cells. The rotors are placed in two different cylindrical grids sliding one over the other. These two grids are embedded into a stationary larger cylindrical grid that extends to 13R in the radial direction, 13R above and 40R below.

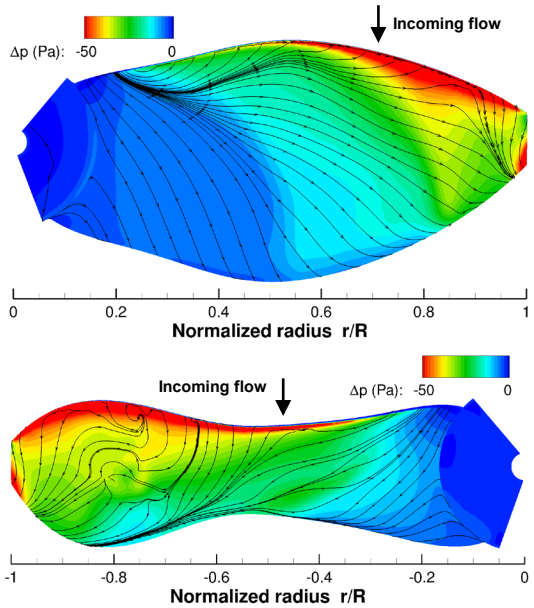

Figure 28. Optimized coaxial configuration. Surface pressure and friction lines on upper and lower rotors.

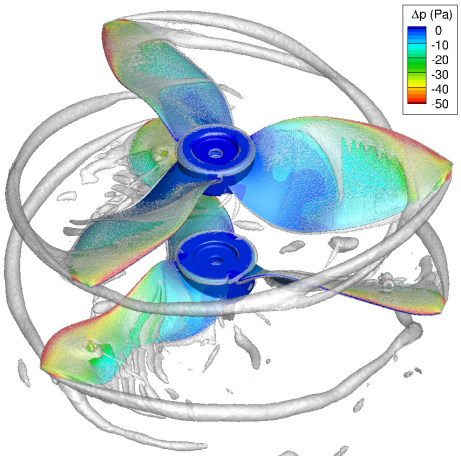

Figure 29. 200 g total thrust coaxial configuration. Q-criterion and surface pressure.

The wall pressure and friction lines on the upper side of the upper and lower rotors are shown in Figure 28 and the iso-surfaces of Q-criterion in Figure 29. On the upper rotor, the pressure and friction lines patterns are almost similar to the

isolated rotor simulation. As said previously, the rotor spacing h/R of 0.5 is sufficient to minimize the influence of the lower rotor on the upper one. The tip vortex and the LEV are still visible on the Q-criterion visualization, merging rapidly in the wake. In this simulation, the vortices do not dissipate immediately. This is due to the unstructured grid that is more refined in the wake, compared to the isolated rotor simulation and the structured grid.

On the lower rotor, the deflection of the friction lines shows a strongly three dimensional flow despite the higher aspect ratio of this blade compared to the upper rotor. The boundary layer separates at trailing edge in the region between 50% and 85% span. It provides wake flow instabilities as seen on the Q-criterion visualization. At about 75% span, in the middle of the blade chord, a small 3D flow separation is visible on the Q-criterion. This phenomenon is caused by the tip vortex of the upper rotor impacting the lower blade, because of upper wake contraction. Note that the FVM solver is able to capture the wake contraction, so the interaction between the lower blade and the upper wake and tip vortex are taken into account in the optimization process. As for the upper rotor, the surface pressure is well distributed all over the blade and no pressure peak occurs at the tip because of the low twist in this region, providing a weak tip vortex and lowering the induced loss.

LOW PRESSURE EXPERIMENTS

Facility and test bench

In order to validate the results from the optimization process, the optimized rotors and some validation cases are manufactured and tested in conditions close to the Martian atmosphere in ONERA's low pressure chamber (Figure 30). It has a volume of 18 m^3, is able to maintain pressure down to 10 Pa and to be filled with CO_2 for building atmospheric conditions closer to Mars. However, it does not replicate perfectly Martian conditions because it runs at ambient temperature. Tests are thus performed at a higher pressure compared to Mars (about 2000 Pa in air and 1000 Pa in CO_2) to reproduce the same Reynolds numbers on the blades.

Figure 30. ONERA's low pressure chamber.

The facility is equipped with a test bench manufactured at ISAE-SUPAERO, placed in the main test chamber, which is about 2 m diameter and 3 m long. The wake of the rotor is directed towards a long cylindrical chamber of about 1 m diameter and 10 m long to minimize flow recirculation. Thrust and torque are measured at rotational speeds up to 16,000 rpm thanks to Faulhauber 4490 H 024B brushless motors. Two set-ups are used: one for single rotors (Figure 31); the other for coaxial rotors (Figure 32). The coaxial set-up is a duplication of the single rotor set-up, in order to make the measurements on upper and lower rotor independent. Forces are measured through load cells with thin-film strain gauges. One is placed on the movable top of the assembly for thrust measurement, with a capacity of 10 N; the second one is placed at the bottom of the rotor-motor assembly for torque measurement, with a capacity of 50 N. A lever arm is used to enlarge the measured efforts and to be able to capture small variations. Electronic signal from the gauge is linearly linked to the movement of the assemblies and to the force. Calibration is performed carefully, considering the expected very low values of thrust and torque. Force measurements are acquired at a frequency of 10 kHz during 10 s, which ensures statistical convergence (Désert, Ref. 22). In addition, each measurement is performed two or four times and reported values are obtained by averaging these measurements. Data accuracy is estimated from the maximum deviation of each measurement to the global average and from discrepancies between measurements and calibration weights (under standard, atmospheric pressure conditions). It was evaluated to be below 5% of reported values. Rotors are manufactured by ISAE-SUPAERO using 3D printed molds and are made of three layers of carbon-epoxy composite (0.8 mm thickness) in order to resist to high centrifugal forces. Layers are shifted from each other with an angle of 120° to ensure isotropic structural behavior on each blade. Rotors weight is less than 30 g. They are statically balanced by grinding and coating, but dynamical balancing is not ensured. Large vibrations were measured at some rotational regime corresponding to structural vibration proper modes of the assembly. The 100 g thrust rotor and the 200 g thrust coaxial configuration are visible in Figure 31 and Figure 32.

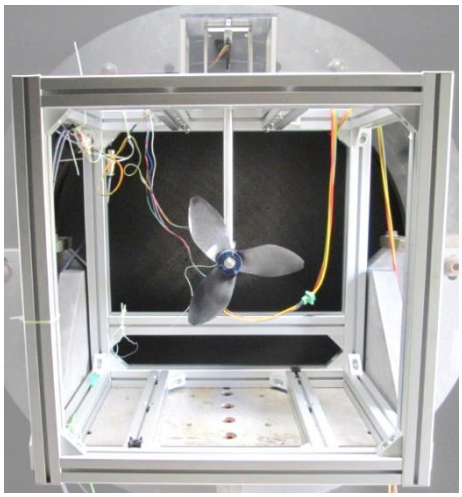

Figure 31. Test bench for the single rotor configuration

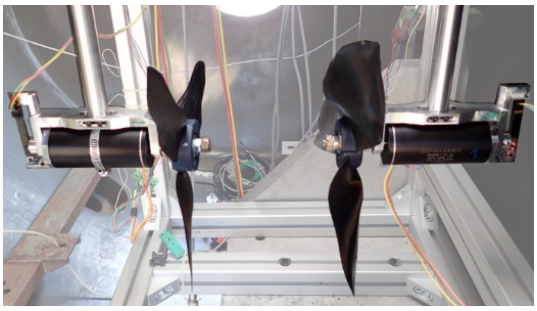

Figure 32. Test bench for the coaxial configuration

Another test bench, presented in Figure 33, was used to measure the effect of a flap, for control considerations, placed in the wake of the coaxial configuration. It consists in a vertical set-up with a suspended carbon-epoxy composite rectangular flat plate of 2 mm thickness, 30 cm span and 5 cm or 10 cm chord (see red frame in the figure). The flap is able to move in two directions, corresponding to drag and lateral (or lift) forces. Two load cells with thin-film strain gauges are attached to the movable parts of the assembly, with complete decoupling of the measured quantities. The flap can be oriented in the wake through discrete angle values (0°, ±5°, ±10° and ±20°), by changing an ad-hoc ring on which the flap is fixed at the top of the assembly. The same calibration and acquisition process as for the two rotors are applied to this set-up.

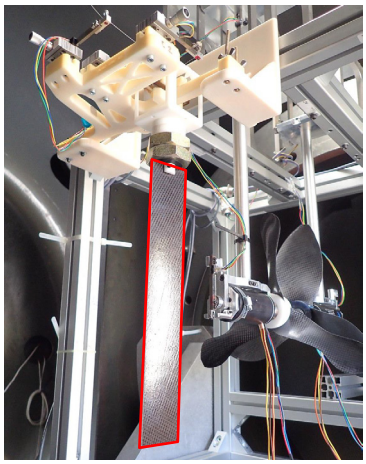

Figure 33. Test bench for the flap configuration.

Validation of measurements

In order to validate the set-up and the force measurements, tests were first performed in ambient conditions on a reference propeller, the Graupner Cam slim 9×6, with well-known characteristics. Verification data are available from UIUC Propeller Data Site and from another test bench used at ISAE-SUPAERO for propellers. The results are not presented here but the new test bench was able to measure fairly well (within 5%) thrust and torque at different rotational speeds. Another validation was performed at low pressure conditions with a rotor tested at the University of Maryland by Shrestha (Ref. 15) in a small evacuation chamber of 0.6 m^3 at the Martian air density of 0.0167 kg/m^3. The rotor, presented in Figure 34, was reproduced carefully. It consists in two rectangular blades of 8.25 in. span and 2 in. chord, attached to the hub of 0.75 in. radius, for a total diameter of 18 in. (about 46 cm). The solidity of the rotor is $\sigma = 0.13$. The airfoil used on the blades is a curved plate with a camber of 6.35% chord and a thickness of 1% chord (0.5 mm). It is made of two layers of carbon-epoxy composite. Hubs are 3D-printed in ABS, with different pitch values. Two pitches of 19° and 30° are considered here.

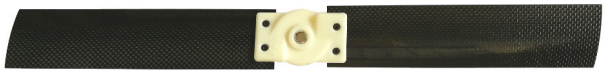

Figure 34. Two-bladed rectangular rotor.

In the present experiments, the air density was about 0.025 kg/m^3 at ambient temperature and low pressure, in order to match the Reynolds number encountered on Mars. Rotational speeds vary from 3000 rpm to 8000 rpm, and chord Reynolds numbers from 5000 to 14,000.

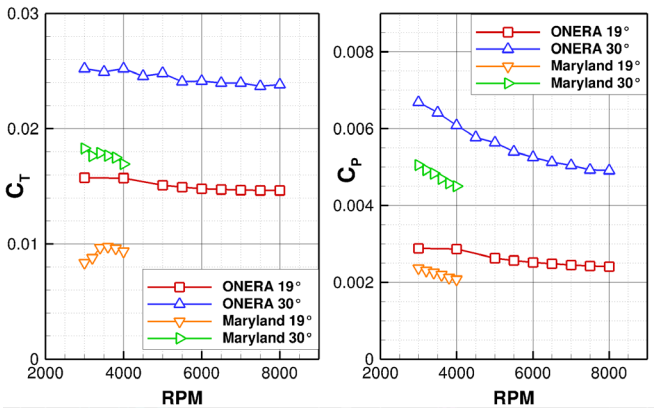

Figure 35. Comparison of measured thrust and torque coefficients on the two-bladed rectangular rotor.

The comparison of thrust and power coefficients between ONERA's and Maryland's experiments is presented in Figure 35. Surprisingly, there are strong differences between the two experiments. The present C_T and C_P are much higher than those obtained by Shrestha, with a 35% to 60% difference. There is a small Reynolds number effect as the air density is different in the two experiments, but this cannot explain such a gap. A more plausible explanation is the recirculation phenomenon. In a 0.6 m^3 chamber, the flow induced by the rotor recirculates and modifies the upstream flow, which decreases the thrust and torque, compared to free boundary air flow. In ONERA's 18 m^3 chamber, recirculation phenomenon is very weak. Comparisons with Tsuzuki experiments (Ref. 17), made in a large chamber comparable to ONERA's, tend to corroborate the present results, in terms of C_T/σ and C_P/σ, even if the tested geometries are slightly different. Navier-Stokes simulations were also performed by Désert (Ref. 24) and show that the present measures of C_T and C_P are 20% and 30% lower than

the computed efforts. These last comparisons give confidence in the present measurements in low pressure conditions. A strong influence of the rotational speed is noticed on power consumption C_P. This is a Reynolds number effect: the increase of *Re* tends to decrease viscous drag and power consumption. Theoretically, the tendency should be inverted for C_T: the increase of *Re* tends to increase the local lift coefficients on the blade as well as the rotor thrust. However, the measurements show a small decrease of C_T with the rotational speed. This phenomenon could come from a slight deformation of the geometry under centrifugal forces, as the blades are not perfectly stiff.

Influence of airfoil geometry

In low Reynolds number flows, the physical behavior of the flow is strongly dependent on the rotational effects. Therefore, it is important to evaluate the optimized airfoil, the 6% cambered plate and the dragonfly airfoil with a similar planform (see Figure 8). The previously evaluated two-bladed rectangular rotor is used at a constant pitch of 19°. The 6% cambered plate airfoil is considered close enough from the 6.35% cambered plate of the rotor manufactured for validation purpose. Two more rotors were built with a 3D-printed stereolithographic technique in order to have a great precision on the complex airfoil shapes. Their structural resistance is however much lower than the carbon-epoxy rotor, and the rotational speed had to be limited to 4000 rpm.

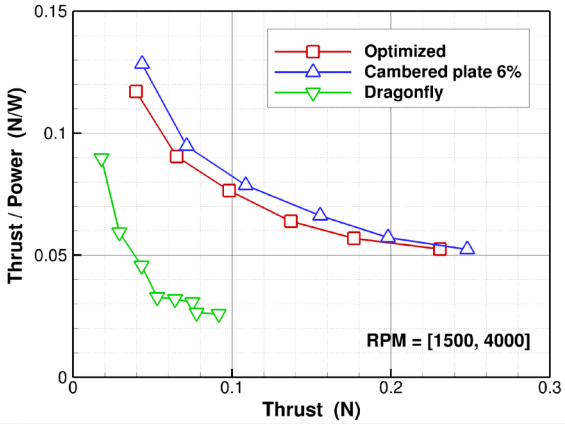

Figure 36. Influence of airfoil on two-bladed rectangular rotor at 19° pitch. ρ = 0.014 kg/m^3.

Figure 36 presents the influence of airfoil geometry on the efforts generated by a rectangular rotor in air at a pressure of 2100 Pa and a density of 0.0245 kg/m^3 for Reynolds number equivalence with Mars. The measured forces are transformed into C_T and C_P coefficients using the experimental density, and extrapolated to the chosen value of Martian density in this study (0.014 kg/m^3). The figure shows the evolution of power-loading T/P plotted against the generated thrust, from 1500 rpm to 4000 rpm. The rotor shaped with the dragonfly section exhibits poor performance, either in thrust capability or in power-loading. This result confirms that a corrugated airfoil is not adapted to a rotating rotor in hover. The rotor shaped with the optimized airfoil exhibits slightly lower performance than the rotor shaped with the cambered plate airfoil, contrarily to the previous 2D analysis. This difference could be caused by the occurrence of a 3D phenomenon, like a LEV, behaving differently according to the shape of the airfoil, or by a different behavior of the dynamic shape of the rotor with the different building process and material. However, the curves join at the highest rotational speed and it seems that the optimized airfoil could be better for higher rotation regime. This result confirms that highly cambered and thin airfoils are the most performant airfoils for rotors rotating in low density conditions. The design thrust of 0.37 N, equivalent to 100 g on Mars, cannot be obtained with the two-bladed rotor for rotational speed below 4000 rpm.

Influence of optimization method

The previous Navier-Stokes analysis of rotors has shown that the use of a FVM method provides rotor geometries with better performance compared to BEMT method. This theoretical result has to be confirmed through experiments. FVM optimized rotors were tested in low pressure conditions in air at a pressure of 2100 Pa and a density of 0.0245 kg.m^3. The different rotors geometries are presented in Figure 37. For comparison, a standard propeller of 30 cm diameter (APC 12.25×3.75), used on terrestrial drones, was also tested in the low pressure chamber.

Figure 37. Tested rotors. From left to right: APC, BEMT opt. (100 g), FVM opt. (100 g), FVM opt. (300 g)

The comparison of efforts generated by the rotors are presented in Figure 38 with the extrapolated thrust in Martian conditions (ρ = 0.014 kg/m^3), in Figure 39 with the thrust coefficient C_T and in Figure 40 with the ratio of the thrust coefficient to the power coefficient C_T/C_P. The rotational speed goes from 4000 rpm to 12,000 rpm. At low rotational speeds, aerodynamic forces are very small and the measurements cannot be considered accurate enough. Standard terrestrial propellers, like APC, cannot achieve sufficient performance for a Martian MAV: thrust is only 0.13 N at 10,000 rpm, with a C_T of only 0.005. On the other hand, optimized rotors provide significant improvements compared to the terrestrial rotor. Considering only the C_T/C_P ratio would tend to recognize the BEMT optimized rotor as the most aerodynamically efficient. However, this rotor generates low thrust, with 0.47 N at 10,000 rpm and a C_T of 0.19. The goal of 0.37 N thrust on Mars is reached at 8800 rpm, which is higher than predicted theoretically with the BEMT method (7500 rpm). The FVM optimized rotor for 100 g thrust has almost 50% more thrust capabilities at

equivalent rotational speed, proving the interest of the FVM method to design rotors. It reaches 0.37 N of thrust at 7000 rpm, which is a little higher than predicted with the FVM method (6100 rpm). The measured C_T value of 0.03 is 25% lower than the one predicted by FVM or Navier-Stokes simulation (0.04, see Table 2) but the C_T/C_P ratio is similar. This difference experiments/simulation could be explained by a slight deformation of the real geometry, compared to the theoretical one, either due to an imperfection in the molding process or to centrifugal forces. Finally, the FVM optimized rotor for 300 g thrust has the best thrust capabilities. The goal of 1.11 N thrust on Mars is reached at 10,000 rpm, which is in good agreement to the predicted value of 9600 rpm. The C_T value of 0.045 is in good agreement of the FVM predicted value of 0.049 (see Table 2). Its C_T/C_P ratio is lower than the optimized rotors for a 0.37N thrust (around 4), but is still higher than the standard propeller.

For the FVM optimized rotors, C_T decreases slightly with the rotational speed. One possible explanation is a deformation of the geometry of the blades under centrifugal forces. This effect could be increased on FVM optimized rotors by the large chords and the large twist on the outer part of the blade. A numerical investigation showed that the same order of magnitude of C_T decrease is achieved with a linear twist decrease along the blade attaining 3° at blade tip for 10,000 rpm. The centrifugal forces are very important: they were estimated to a load of 120 kg at 12,000 rpm for the largest FVM rotor blade weighing 9 g. For the BEMT optimized rotor, the centrifugal force is only 65 kg at the same rotational speed for a blade weighing 5.7 g, and a shape more resistant to deformation compared to FVM blades. This explains the constant C_T value on BEMT rotor, whatever the rotational speed, as on APC rotor. With FVM optimized rotors, the power needed to thrust 100 g and 300 g on Mars is 10 W and 45 W, respectively. These values are easily attainable with small electric motors.

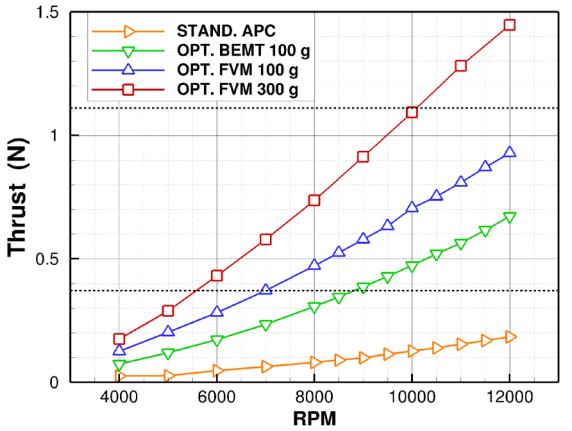

Figure 38. Comparison of optimized rotors on thrust in Martian conditions. ρ = 0.014 kg.m^3.

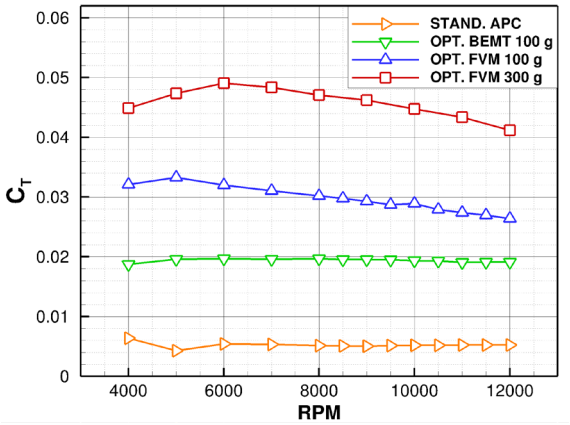

Figure 39. Comparison of optimized rotors on C_T.

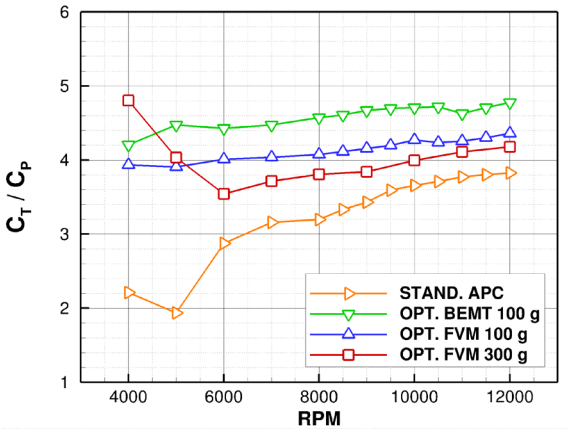

Figure 40. Comparison of optimized rotors on C_T/C_P.

Influence of gas

The effect of atmospheric characteristic was also investigated. First, it is important to check if the nature of the gas, air or CO_2, has an effect on the performance. The sound velocity differing with gas composition, it is crucial to compare the results for a given tip Mach number instead of a given rotational speed. Furthermore, experiments were carried out in air and CO_2 at different pressures to maintain identical Reynolds number. The performance of the FVM optimized rotor (100 g thrust) is presented in Figure 41, in terms of C_T and C_T/C_P ratio versus the tip Mach number. The maximal rotational speed is here 16,000 rpm, corresponding to $M_{tip} = 0.71$ in air and $M_{tip} = 0.91$ in CO_2. It is noted that very high vibration levels were measured at high rotational speed that could have impacted the measure itself. The phenomenon is probably due to the unperfected dynamical balancing of the rotor. However, it can be considered from the measured that the nature of the gas has little influence on the behavior of the efforts, in agreement with previous observations (Munday, Ref. 16). It is observed that the thrust coefficient drops significantly for $M_{tip} = 0.5$ without impacting the value of C_T/C_P. An inflexion of the curve is visible beyond $M_{tip} = 0.7$ where the C_T/C_P ratio is surprisingly increasing. One could have expected that transonic effects would have drastically increased the power

consumption and decreased the C_T/C_P ratio. This result is in agreement with the previous Navier-Stokes simulations performed on the FVM optimized rotor in transonic and supersonic tip flow regime, in which neither power divergence nor thrust drop occur. This means that the rotor can be operated over a large rotational speed range, up to transonic tip Mach number.

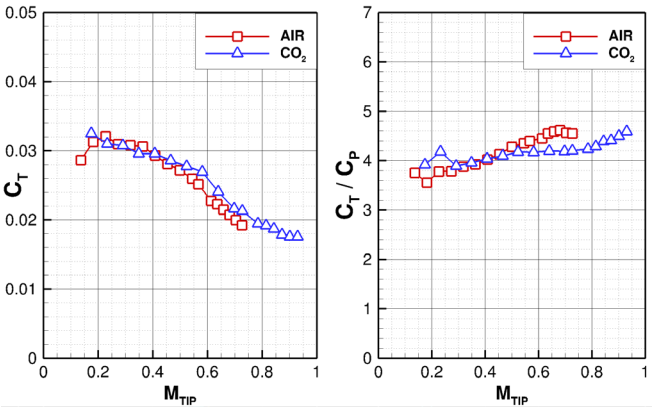

Figure 41. Effect of gas composition on rotor performance (FVM opt. 100 g). C_T and C_T/C_P vs. M_{tip}.

Influence of density

The effect of density, or consequently the effect of the Reynolds number, is now addressed by varying the pressure of the chamber. Tests were performed in air at ambient temperature and at pressure values of 20, 100, 500, 1000 hPa (ambient). These pressure values correspond on Earth to density conditions found respectively at about 30, 20, 10 and 0 km altitude.

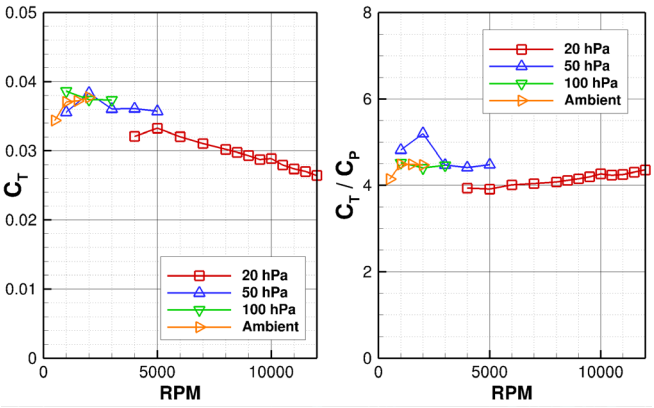

Figure 42. Effect of density on rotor performance (FVM opt. 100 g). C_T and C_T/C_P vs. rotational speed.

Measured efforts are presented in Figure 42. Quite surprisingly, density has little influence on thrust and power coefficients using an airfoil and rotor geometry optimized for Reynolds numbers below 10^4 corresponding to laminar flow. Considering the blade chord of 7 cm at $0.7R$ and a rotational speed of 4000 rpm, the chord Reynolds numbers are respectively 4000, 20,000, 90,000 and 180,000. The boundary layer flow probably becomes turbulent above $Re = 20{,}000$, but the rotor still exhibits a C_T value of 0.036 and a C_T/C_P value of 4.5, close to the values for ultra-low Reynolds numbers. This result proves again the great operability of the optimized rotor.

Coaxial configurations

For a coaxial configuration, upper and lower rotors are assumed to rotate at the same speed and to produce the same torque (equal in magnitude and opposite in sign), in order to equilibrate the configuration. FVM evaluations showed that, in this case, the rotors do not produce the same thrust: it was estimated that the lower rotor has a thrust reduced by 17% to 20% compared to the upper one. It is important to verify these numbers by measurements. Tests are carried out as following: for each rotational speed of the upper rotor, three values of rotational speed are set for the lower rotor, and thrust and torque are measured for both rotors. Then the speed of the lower rotor permitting to match the torque of the upper rotor is interpolated within the three values (assuming a theoretical Ω^2 behavior of the torque). Then corresponding thrust and rotational speed are deduced. Both coaxial configurations for 200 g and 600 g were measured in low pressure conditions. Torque, thrust and power evolutions with the rotational speed are presented in Figure 43, Figure 44 and Figure 45 respectively, for Martian conditions at $\rho = 0.014$ kg/m^3. Contrarily to the design, at given rotational speed, torques for the upper and lower rotors are not equal. The differences are higher for the 200 g coaxial configuration than for the 600 g one. The black dots on the figures correspond to the design total thrust of the configurations, deduced by linear interpolation of the measurements. For the Martian 200 g total thrust (0.74 N), upper and lower rotor rotate at 7250 rpm and 6000 rpm, respectively, instead of the design value of 6100 rpm. At these rotational speeds, the thrust on upper and lower rotors are 0.44 and 0.30, respectively. The lower rotor generates 32% less thrust than the upper rotor. The corresponding power values are respectively 12.5 W and 10.5 W, equaling to 23 W for the full coaxial configuration, a quite low value for a Martian MAV.

In order to attain the Martian 600 g of total thrust (2.22 N), upper and lower rotor rotate respectively at 9900 rpm and 9000 rpm, which is close to the design value of 9600 rpm. In this case, the corresponding thrust values are respectively 1.27 N and 0.95 N, meaning 25% less thrust for the lower rotor. This measured difference is close to the value predicted numerically. The corresponding power values are respectively 51 W and 47 W, equaling to 98 W for the full coaxial configuration. This value may seem too large for a Martian MAV for the question of battery sizing and recharge. However, considering a total lifted mass of 600 g for a vehicle of only 30 cm diameter, the measured performance is very encouraging.

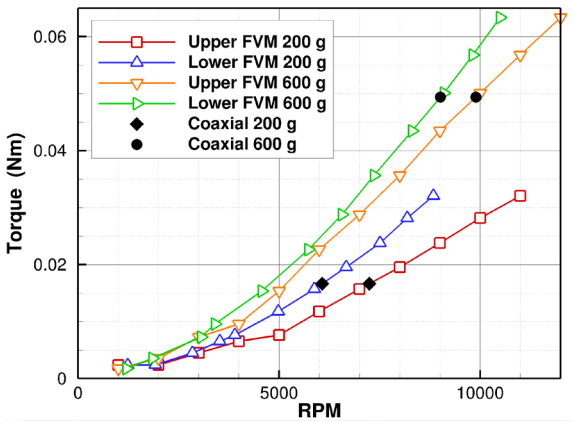

Figure 43. Comparison of coaxial configurations. Torque vs. rotational speed. ρ = 0.014 kg/m^3.

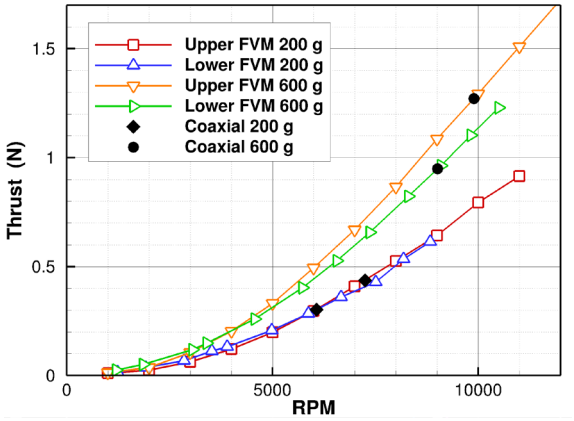

Figure 44. Comparison of coaxial configurations. Thrust vs. rotational speed. ρ = 0.014 kg/m^3.

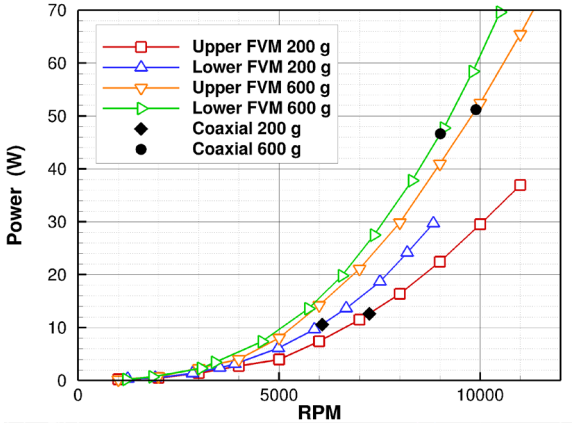

Figure 45. Comparison of coaxial configurations. Power vs. rotational speed. ρ = 0.014 kg/m^3.

Flap measurements

In helicopters, control is usually made through pitch and articulated blades at the hub, involving complex and heavy mechanical systems. It is hardly possible here considering the high inertia of the blades. Another way is to directly control the thrust direction by tilting the plane of one or two rotors. This involves placing the rotors and the motors on an articulated assembly, which again adds complexity and weight to the system. A simple and efficient way is to control the MAV laterally through two orthogonal flaps piloted by servomotors. The last two controls, altitude and rotation, could be made through independent management of each rotor's rotational speed. Tests were thus performed with a flap placed in the wake of the coaxial configuration. The flap set-up was already presented in Figure 33. Two flaps of different chords (5 cm and 10 cm) were tested, but only the flap of 5 cm chord is presented here. The flap was placed in the wake of the coaxial configuration with 200 g total thrust. With the experience from the previous experimentations, the rotational speeds of the two rotors were chosen to reproduce a torque equilibrated configuration, following the numbers presented in Figure 43. The evolutions of the lift and drag forces with the angle of attack are presented in Figure 46 in low pressure conditions and recalculated for the Martian density of 0.014 kg/m^3. The rotational speed chosen to plot the results is the upper one. Aerodynamic forces seem to evolve as the square of the rotational speed, as expected. Lift values are opposite for opposite angles of attack, and drag values are equal in this case. The angle of attack of 20° is usually beyond stall for wings at high Reynolds number. However, stall is not happening in Martian atmospheric conditions. A separation probably occurs considering the high value of the drag and the large fluctuations observed in the experiments (not shown here). A flap angle of 10° should be the maximum value to consider for control in order to produce sufficient lateral force without excessive drag penalty.

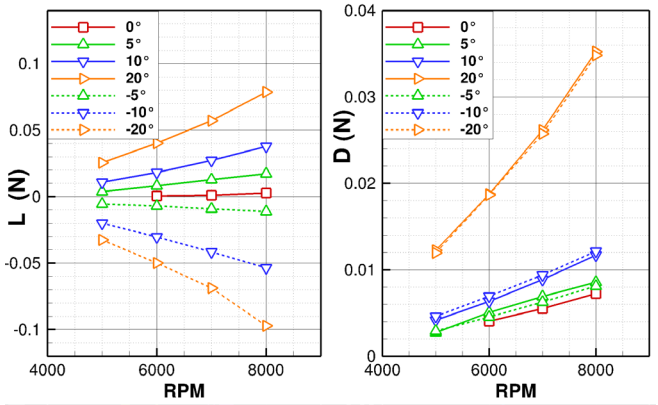

Figure 46. Effect of the angle of attack on lift and drag. Flap of 5 cm chord. ρ = 0.014 kg/m^3.

In order to extrapolate these numbers to a completely new configuration, it is important to model the behavior of the flap. The aerodynamic coefficients can be first calculated, knowing the reference surface S_{ref} and the reference velocity V_{ref}. S_{ref} is naturally the surface of the flap. V_{ref} is characteristic of the wake induced flow, function of the thrust of the rotors. It can be logically deduced from the expression of the induced velocity given by Froude's theory for a helicopter in hover:

$$V_i = \Omega R \sqrt{\frac{C_T}{2}}$$

For a coaxial configuration however, both rotors have to be considered, with their different rotational speeds and thrust coefficients. The best way to respect the physical properties of the flow is to take the quadratic average of both induced velocities on upper (subscript u) and lower (subscript l) rotors:

$$V_{ref} = \sqrt{V_{i_u}^2 + V_{i_l}^2} \text{ with } V_{i_u} = \Omega_u R \sqrt{\frac{C_{T_u}}{2}} \; ; \; V_{i_l} = \Omega_l R \sqrt{\frac{C_{T_l}}{2}}$$

Using the previous expressions, the resulting lift and drag coefficients are presented in Figure 47. C_L and C_D are almost constant with rotational speed, which is satisfactory and validates the assumptions made for the reference velocity computation.

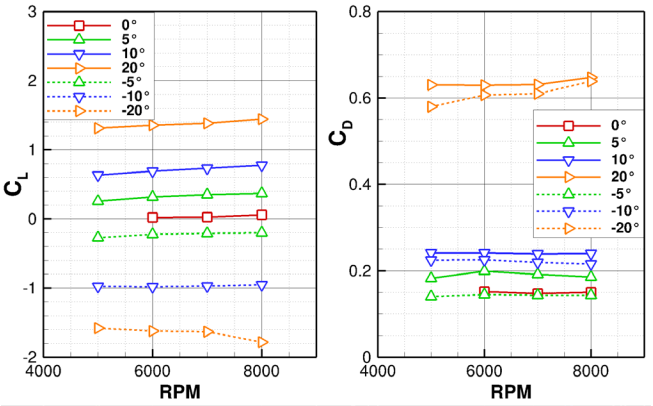

Figure 47. Effect of the angle of attack on lift and drag coefficients. Flap of 5 cm chord.

It is now possible to model the aerodynamic coefficients using the classical theory for wings:

$$C_L = K_1 \frac{2\pi\alpha}{1+2/AR} \; ; \; C_D = K_2 C_{D_0} + K_3 \frac{C_L^2}{\pi AR}$$

with α in rad, C_{D0} is the viscous drag coefficient and K_1, K_2, K_3 some correction coefficients for measurement fitting. The viscous drag coefficient can be expressed following laminar boundary layer theory for a flat plate with a correction coefficient from airfoil theory:

$$C_{D_0} = K \frac{2.656}{\sqrt{Re_c}} \text{ with } K = 1 + 2\frac{t}{c} + 60\left(\frac{t}{c}\right)^4$$

After a calibration based on the present experiments, the following correction coefficients are found:

$$K_1 = 0.9 \; ; \; K_2 = 2 \; ; \; K_3 = 2$$

The correction K_1 on the lift coefficient is logical because the slope of the curve $C_L = f(\alpha)$ is decreasing in case of low Reynolds numbers. The correction on the drag is quite important, meaning that some effects are not taken into account. The behavior of a flap in a rotor wake is far from being similar to a wing in a constant upstream flow. Firstly, the flap is partially immersed in the induced flow (around 70% span) because of the wake contraction. Secondly, the induced velocity expression is based on Froude's theory, which could not represent accurately the wake of the present coaxial configuration. Finally, there could be additional drag sources due to local boundary layer separations in some part of the flap. However, at this level of design, the proposed model for the aerodynamic behavior of the flap is satisfactory.

PRELIMINARY DESIGN OF A MARTIAN VTOL MAV

The experimental results can be used for a preliminary design of a Martian VTOL MAV, based on existing technologies for terrestrial drones: carbon composite rotors and structure, brushless motors, electronic speed controller (ESC), LiPo battery, servomotors, flight controller, emitter-receiver, camera. Figure 48 presents a possible design of such a vehicle.

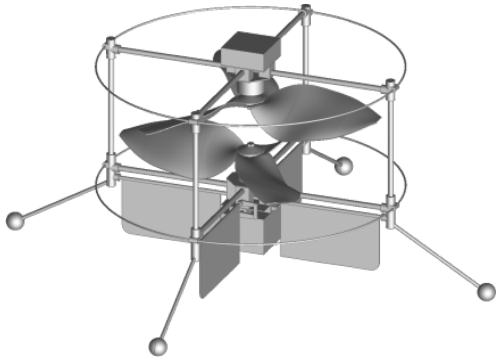

Figure 48. Example of a Martian coaxial VTOL MAV

The experimental results can be extrapolated to design any prescribed mass resulting from a reasonable mass budget for the different elements of the MAV. The 200 g total mass of the coaxial configuration was used initially as a basis for design, but seems hardly feasible. After a few design iterations, a total mass of 500 g seems more realistic, based on the budget presented in Table 3.

Table 3: Mass budget (g) of a coaxial rotor Martian MAV with a total mass of 500 g.

2×rotors	2×motors	2×ESC	Battery	Structure
50	100	20	150	120
2×servos	Controller	Emitter	Receiver	2×cameras
10	20	10	10	10

A mass of 500 g needs a 1.86 N thrust in Martian gravity. Considering the mean daytime density of 0.0167 kg/m^3, the thrust can be achieved by the optimized coaxial configuration with rotational speeds of 8900 rpm and 8200 rpm for upper and lower rotors respectively. The needed corresponding total power is 76 W. Considering a motor mechanical efficiency of 75%, a battery energy mass

ratio of 160 Wh/kg and a battery managing system limiting its available capacity to 80%, a battery mass of 150 g could achieve a flight duration of about 12 min, which is enough to take-off, climb to a few tens meter altitude, explore the surroundings within a few hundred meter around the rover and land. The lateral control could be obtained through two flaps as described previously. Based on the aerodynamic model, for a chord of 10 cm and a flap angle of 10°, the lateral and drag forces are estimated respectively to 6% and 1.7% of the total thrust. A representation of the flight dynamics of the MAV is necessary to know if the present lateral force could be sufficient to effectively control the vehicle.

CONCLUSION AND PERSPECTIVES

This paper shows the methodology to attain a feasible design of airfoils and rotors optimized for a vertical take-off and landing micro aerial vehicle in Martian atmosphere, where laminar compressible ultra-low Reynolds number flows occur. The free vortex method used in the rotor optimization process is able to accurately take into account the effect of the wake induced velocities on the performance of the rotor, either in isolated or coaxial configuration. This method compares well with more advanced unsteady laminar Navier-Stokes simulations, which is not the case of the simpler blade element momentum theory. ONERA's low pressure chamber associated to ISAE-SUPAERO's test bench provided a large data base on thrust and power capacities of isolated and coaxial rotors over a large range of rotational speeds, confirming the aerodynamic efficiency of the optimized rotors. Surprisingly, the rotor remains aerodynamically efficient up to transonic speed at blade tip, which was demonstrated both in experiments and simulations, and up to ambient pressure, i.e. high Reynolds numbers. The proposed prototype needs deeper system analysis: the association rotor+motor+ESC is essential and preliminary tests with existing components show that managing such high inertia rotors is not straightforward. In the future, a full prototype will be manufactured and tested in Earth gravity in the low pressure chamber at different pressure levels to assess the present concept of a coaxial rotor VTOL MAV for Martian exploration.

Author contact: Hervé Bézard herve.bezard@onera.fr,
Thierry Jardin thierry.jardin@isae.fr,
Jean-Marc Moschetta jean-marc.moschetta@isae.fr.

ACKNOWLEDGMENTS

The authors would like to thank M. Saccoccio and G. Doulsier from CNES for their support of the experimental campaign, R. Chanton, H. Dedieu, S. Belliot and X. Foulquier from ISAE-SUPAERO for the rotor manufacturing and the test bench, J.P. Brazier from ONERA for the linear stability analysis and C. Corato from ONERA for the facility management.

REFERENCES

1. Braun, R., Wright, H., Croom, M., Levine, J.S., and Spencer, D., "Design of the ARES Mars Airplane and Mission Architecture," *Journal of Spacecraft and Rockets*, Vol. 43, (5), 2006.
2. Kerzhanovich, V.V., Cutts, J., Cooper, H., Hall, J., McDonald, B., Pauken, M., White, C., Yavrouin, A., Castano, A., Cathey, H., Fairbrother, D., Smith, S., Shreves, C., Lachenmeier, T., Rainwated, E., and Smith, M., "Breakthrough in Mars balloon technology," *Advances in Space Research*, Vol. 33, (10), 2004, pp. 1836-1841.
3. Balaram, J. and Tokumaru, P.T., "Rotorcrafts for Mars exploration," 11th International Planetary Probe Workshop, Pasadena, California, USA, 2014.
4. Balaram, J., Canham, T., Duncan, C., Golombek, M., Grip, H.F., Johnson, W., Maki, J., Quon, A., Stern, R., and Zhu, D., "Mars Helicopter Technology Demonstrator," AIAA Atmospheric Flight Mechanics Conference, Kissimmee, Florida, January 8-12, 2018.
5. Kunz, P.J., "Aerodynamics and Design for Ultra-Low Reynolds Number Flight," Ph.D. Thesis, Stanford University, USA, 2003.
6. Liu, Z., Albertani, R., Moschetta, J., Thipyopas, C., and Xu, M., "Experimental and Computational Evaluation of Small Microcoaxial Rotor in Hover," *Journal of Aircraft*, Vol. 48, (1), 2011, pp. 220-229.
7. Bohorquez, F., "Rotor Hover Performance and System Design of an Efficient Coaxial Rotary Wing Micro Air Vehicle," Ph.D. thesis, University of Maryland, 2007.
8. Drela, M., "XFOIL: An Analysis and Design System for Low Reynolds Number Airfoils," *Low Reynolds Aerodynamics*, Edited by Mueller, T.J., Springer Verlag, 54, Berlin, Germany, 1989, pp. 1-12.
9. Leishman, J., and Ananthan, S., "Aerodynamic optimization of a coaxial proprotor," American Helicopter Society 62th Annual Forum Proceedings, Phoenix, AZ, USA, May 9-11, 2006.
10. Song, H., and Underwood, C., "A Mars VTOL Aerobot - Preliminary Design, Dynamics and Control," IEEE Aerospace Conference, Vols. 1-9, 2007, pp. 1-14.
11. Lakshminarayan, V., and Baeder, J., "Computational Investigation of Microscale Coaxial-Rotor Aerodynamics in Hovers," *Journal of Aircraft*, Vol. 47, (3), 2010.
12. Liu, Z., Albertani, R., Moschetta, J.M., Thipyopas, C., and Xu, M., "Experimental and Computational Evaluation of Small Microcoaxial Rotor in Hover," *Journal of Aircraft*, Vol. 48, (1), 2011, pp. 220-229.
13. Young, L., Derby, M., Demblewski, R., and Navarrete, J., "Experimental Investigation and Demonstration of Rotary-Wing Technologies for Flight in the Atmosphere of Mars," 58th Annual Forum of the AHS, Montreal, Canada, June 11-13, 2002.
14. Corfeld, K., Strawn, R., and Long, L.N., "Computational Analysis of a Prototype Martian Rotorcraft Experiment," Paper AIAA-2002-2815, 20th AIAA Applied Aerodynamics Conference Proceedings,

St. Louis, Missouri, USA, 2002.
15. Shrestha, R., Benedict, M., Hrishikeshavan, V., and Chopra, I., "Hover Performance of a Small-Scale Helicopter Rotor for Flying on Mars," *Journal of Aircraft*, Vol. 53, (4), 2016, pp. 1-8.
16. Munday, P., Taira, K., Suwa, T., Numata, D., and Asai, K., "Nonlinear Lift on a Triangular Airfoil in Low-Reynolds-Number Compressible Flow," *Journal of Aircraft*, Vol. 52, (3), 2015, pp. 924-931.
17. Tsuzuki, N., Sato, S. and Abe, T., "Design Guidelines of Rotary Wings in Hover for Insect-Scale Micro Air Vehicle Applications," *Journal of Aircraft*, Vol. 44, (1), 2007.
18. Ament, G.A., and Koning, W.J.F., "Isolated Rotor Forward Flight Testing From One Atmosphere Down to Martian Atmospheric Densities," AHS International Technical Conference on Aeromechanics Design for Transformative Vertical Flight, San Francisco, CA, January 16-18, 2018.
19. Millour, E., Forget, F., Spiga1, A., Vals, M., Zakharov, V., Montabone, L., Lefèvre, F., Montmessin, F., Chaufray, J.Y., López-Valverde, M. A., González-Galindo, F., Lewis, S. R., Read, P. L, Desjean, M.C., and Cipriani, F., "The Mars Climate Database (Version 5.3)," Scientific Workshop: From Mars Express to ExoMars, ESAC, Madrid, Spain, February 27-28, 2018.
20. Leovy, C., "Weather and climate on Mars," *Nature*, Vol. 412, 2001, pp. 245–249.
21. Bézard, H., and Moschetta, J.-M., "Aerodynamic Design of a Rotary-Wing Micro Air Vehicle for Flying on Mars," *Space Robotics Symposium*, Glasgow, UK, 2015.
22. Désert, T., "Étude aéropropulsive d'un micro-drone à voilure tournante pour l'exploration martienne," Ph.D. Thesis, ISAE-SUPAERO, University of Toulouse, France, 2019.
23. Cambier, L., Gazaix, M., Heib, S., Plot, S., Poinot, M., Veuillot, J.-P., Boussuge, J.-F., and Montagnac, M., "An overview of the multi-purpose *elsA* flow solver," *Journal Aerospace Lab*, Vol. 2, 2011, pp. 1-15.
24. Désert, T., Jardin, J., Bézard, H., and Moschetta, J.M., "Numerical predictions of low Reynolds number compressible aerodynamics," *Aerospace Science and Technology*, Vol. 92, 2019.
25. Désert, T., Moschetta, J.M., and Bézard, H., "Numerical and experimental investigation of an airfoil design for a Martian micro rotorcraft," *International Journal of Micro Air Vehicle*s, Vol. 10, (3), 2018, pp. 262-272.
26. Kulfan, B.M., and Bussoletti, J.E., "Fundamental" parametric geometry representations for aircraft component shapes," In 11th AIAA/ISSMO Multidisciplinary Analysis and Optimization, 2006.
27. Kesel, A., "Aerodynamic Characteristics of Dragonfly Wing Sections compared with Technical Aerofoils," *The Journal of Experimental Biology*, Vol. 203, 2000, pp. 3125-3135.
28. Drela, M., "QPROP", http://web.mit.edu/drela/Public/web/qprop, 2007.
29. Le Bouar, G., Costes, M., Leroy-Chesneau, A., Devinant, P., "Numerical simulations of unsteady aerodynamics of helicopter rotor in maneuvering flight conditions," *Aerospace Science and Technology*, Vol. 8, 2004, pp. 11-25.